



Characterizing the Fast Radio Burst Host Galaxy Population and its Connection to Transients in the Local and Extragalactic Universe

Shivani Bhandari¹ , Kasper E. Heintz^{2,3} , Kshitij Aggarwal^{4,5} , Lachlan Marnoch^{1,6,7} , Cherie K. Day^{1,8} , Jessica Sydnor^{4,5} , Sarah Burke-Spolaor^{4,5,9} , Casey J. Law^{10,11} , J. Xavier Prochaska^{12,13} , Nicolas Tejos¹⁴ , Keith W. Bannister¹ , Bryan J. Butler¹⁵ , Adam T. Deller⁸, R. D. Ekers¹ , Chris Flynn⁸ , Wen-fai Fong¹⁶ , Clancy W. James¹⁷ , T. Joseph W. Lazio¹⁸, Rui Luo¹, Elizabeth K. Mahony¹ , Stuart D. Ryder^{6,7} , Elaine M. Sadler^{1,19} , Ryan M. Shannon⁸ , JinLin Han^{20,21,22} , Kejia Lee^{20,23} , and Bing Zhang²⁴

¹ CSIRO, Space and Astronomy, P.O. Box 76, Epping, NSW 1710 Australia; shivani.bhandari@csiro.au
² Centre for Astrophysics and Cosmology, Science Institute, University of Iceland, Dunhagi 5, 107 Reykjavík, Iceland
³ Cosmic Dawn Center (DAWN), Niels Bohr Institute, University of Copenhagen, Jagtvej 128, DK-2100 Copenhagen Ø, Denmark
⁴ Department of Physics and Astronomy, West Virginia University, P.O. Box 6315, Morgantown, WV 26506, USA
⁵ Center for Gravitational Waves and Cosmology, West Virginia University, Chestnut Ridge Research Building, Morgantown, WV 26505, USA
⁶ Department of Physics and Astronomy, Macquarie University, NSW 2109, Australia
⁷ Astronomy, Astrophysics and Astrophotonics Research Centre, Macquarie University, Sydney, NSW 2109, Australia
⁸ Centre for Astrophysics and Supercomputing, Swinburne University of Technology, John St, Hawthorn, VIC 3122, Australia
⁹ Canadian Institute for Advanced Research, CIFAR Azrieli Global Scholar, MaRS Centre West Tower, 661 University Ave. Suite 505, Toronto, ON M5G 1M1, Canada
¹⁰ Cahill Center for Astronomy and Astrophysics, MC 249-17 California Institute of Technology, Pasadena, CA 91125, USA
¹¹ Owens Valley Radio Observatory, California Institute of Technology, 100 Leighton Lane, Big Pine, CA 93513, USA
¹² University of California, Santa Cruz, 1156 High St., Santa Cruz, CA 95064, USA
¹³ Kavli Institute for the Physics and Mathematics of the Universe (Kavli IPMU), 5-1-5 Kashiwanoha, Kashiwa, 277-8583, Japan
¹⁴ Instituto de Física, Pontificia Universidad Católica de Valparaíso, Casilla 4059, Valparaíso, Chile
¹⁵ National Radio Astronomy Observatory, Socorro, NM 87801, USA
¹⁶ Center for Interdisciplinary Exploration and Research in Astrophysics (CIERA) and Department of Physics and Astronomy, Northwestern University, Evanston, IL 60208, USA
¹⁷ International Centre for Radio Astronomy Research, Curtin University, Bentley, WA 6102, Australia
¹⁸ Jet Propulsion Laboratory, California Institute of Technology, Pasadena, CA 91109, USA
¹⁹ Sydney Institute for Astronomy, School of Physics A28, The University of Sydney, NSW 2006, Australia
²⁰ National Astronomical Observatories, Chinese Academy of Sciences, 20A Datun Road, Chaoyang District, Beijing 100012, People's Republic of China
²¹ CAS Key Laboratory of FAST, NAO, Chinese Academy of Sciences, Beijing 100101, People's Republic of China
²² School of Astronomy, University of Chinese Academy of Sciences, Beijing 100049, People's Republic of China
²³ Kayli Institute for Astronomy and Astrophysics, Peking University, Beijing 100871, People's Republic of China
²⁴ Department of Physics and Astronomy, University of Nevada, Las Vegas, Las Vegas, NV 89154, USA

Received 2021 August 2; revised 2021 November 10; accepted 2021 November 16; published 2022 January 17

Abstract

We present the localization and host galaxies of one repeating and two apparently nonrepeating fast radio bursts (FRBs). FRB 20180301A was detected and localized with the Karl G. Jansky Very Large Array to a star-forming galaxy at $z = 0.3304$. FRB20191228A and FRB20200906A were detected and localized by the Australian Square Kilometre Array Pathfinder to host galaxies at $z = 0.2430$ and $z = 0.3688$, respectively. We combine these with 13 other well-localized FRBs in the literature, and analyze the host galaxy properties. We find no significant differences in the host properties of repeating and apparently nonrepeating FRBs. FRB hosts are moderately star forming, with masses slightly offset from the star-forming main sequence. Star formation and low-ionization nuclear emission-line region emission are major sources of ionization in FRB host galaxies, with the former dominant in repeating FRB hosts. FRB hosts do not track stellar mass and star formation as seen in field galaxies (more than 95% confidence). FRBs are rare in massive red galaxies, suggesting that progenitor formation channels are not solely dominated by delayed channels which lag star formation by gigayears. The global properties of FRB hosts are indistinguishable from core-collapse supernovae and short gamma-ray bursts hosts, and the spatial offset (from galaxy centers) of FRBs is mostly inconsistent with that of the Galactic neutron star population (95% confidence). The spatial offsets of FRBs (normalized to the galaxy effective radius) also differ from those of globular clusters in late- and early-type galaxies with 95% confidence.

Unified Astronomy Thesaurus concepts: Galaxies (573); Radio interferometry (1346); Radio bursts (1339)

1. Introduction

The physical mechanism and the source population(s) powering the energetic (10^{-2} to ~ 400 Jy ms) and μ s–ms

duration fast radio bursts (FRBs) are currently two of the biggest mysteries of modern astrophysics. Significant progress has been made in the last two years, with (sub)arcsecond localization of FRBs using radio interferometers such as the Karl G. Jansky Very Large Array (VLA), the Australian Square Kilometre Array Pathfinder (ASKAP), the Deep Synoptic Array (DSA-10), and the European VLBI Network (EVN; Chatterjee et al. 2017; Bannister et al. 2019b; Ravi et al. 2019; Law et al. 2020; Marcote et al. 2020). These FRB localizations



Original content from this work may be used under the terms of the [Creative Commons Attribution 4.0 licence](https://creativecommons.org/licenses/by/4.0/). Any further distribution of this work must maintain attribution to the author(s) and the title of the work, journal citation and DOI.

have enabled the identification of FRB host galaxies, and in some cases the location of the FRBs within the galaxies, which has provided the clues to the progenitor channels of these enigmatic sources. While the nature of FRBs remains uncertain, the redshifts for localized FRBs still permit us to probe the baryonic content of the universe (Macquart et al. 2020), through measurements of the ionized baryon density in the intergalactic medium. FRBs are thus excellent probes of cosmology and the structure of the universe (Bhandari & Flynn 2021).

Recently, the Canadian Hydrogen Intensity Mapping Experiment Fast Radio Burst (CHIME/FRB) Project published a catalog of 535 FRBs detected during their first year of operations and observed in the range 400–800 MHz (Amiri et al. 2021). The catalog represents the first large sample ($\gg 10^2$) of FRBs detected in a well-controlled experiment. It includes bursts from repeating and nonrepeating FRB sources, and facilitates a comparative study of the FRB population. The CHIME/FRB sample reveals that while the sky locations and dispersion measures (DMs) of the two FRB populations are consistent with being drawn from the same distribution, the bursts from repeating sources have wider pulse widths and narrower bandwidths compared to apparent nonrepeaters (Fonseca et al. 2020; Pleunis et al. 2021). Thus, these observational differences in the bursts themselves hint at different propagation or emission mechanisms for the two FRB subpopulations. Whether all FRBs repeat is still an outstanding question in the field (Palaniswamy et al. 2018; Caleb et al. 2019; James 2019; Ravi 2019; Ai et al. 2021).

In addition to the properties of the bursts, analyses of their host galaxy environments may provide more clues to disentangle the two FRB populations and their progenitor sources (Chittidi et al. 2021; Tendulkar et al. 2021). Currently, 15 FRBs (including repeating and nonrepeating) have been localized to host galaxies at redshifts in the range $z = 0.03$ – 0.66 (Heintz et al. 2020).²⁵ This preliminary sample shows that FRB host galaxies overall exhibit a broad range of color ($u - r = 0.9$ – 2.0), stellar mass ($M_\star = 10^8$ – $10^{10} M_\odot$), and star formation rate ($\text{SFR} = 0.05$ – $10 M_\odot \text{ yr}^{-1}$). Moreover, the burst sites are in most cases significantly offset from the host galaxy centers. A high-spatial-resolution analysis of a subset of FRB hosts found that most FRBs are not located in regions of elevated local star formation and stellar mass surface densities in comparison to the mean global values of their hosts (Mannings et al. 2020). Also, the majority of hosts in Mannings et al. (2020) show clear spiral arm features in the infrared (IR), with the positions of the bursts found to be consistent with an origin in the spiral arms. An analysis of the host-burst offset distribution and other host properties rule out long gamma-ray bursts (LGRBs) and superluminous supernovae (SLSNe) as FRB production channels and favor compact merger events (double white dwarf (WD) and double neutron star (NS) mergers), accretion-induced collapse (AIC) of a white dwarf, and core-collapse supernovae (CCSNe) to be plausible mechanisms for nonrepeating ASKAP-localized bursts (Bhandari et al. 2020; Heintz et al. 2020; Li & Zhang 2020).

In this first, relatively small host galaxy sample, tentative evidence was found for the hosts of the repeating FRBs to be less massive and less luminous on average, compared to the hosts of the apparently nonrepeating FRBs. Even within the

specific subpopulation of repeating FRB hosts, though, a very diverse nature is apparent; FRB20121102A originates in a highly magnetized environment (Michilli et al. 2018) colocated with a radio nebula in a low-metallicity, highly star-forming dwarf galaxy at $z = 0.1927$ (Tendulkar et al. 2016; Chatterjee et al. 2017). The immediate environment and host galaxy properties of the FRB20121102A source led to a concordant model for FRBs in which bursts are produced by young magnetars, remnants from SLSNe or LGRBs (Margalit & Metzger 2018). In contrast, FRB20180916B originates close to a star-forming region in a massive nearby ($z = 0.03$) spiral galaxy (Marcote et al. 2020) lacking an extreme magneto-ionic environment and radio nebula. Observations with the Hubble Space Telescope (HST) established a small but significant offset of FRB20180916B from the nearest knot of active star formation in the host galaxy. This suggests that the age of the progenitor is inconsistent with that of a young magnetar but compatible with the ages of high-mass X-ray binaries and gamma-ray binaries (Tendulkar et al. 2021). Another repeating source, FRB20200120E, is localized to a globular cluster system in the nearby spiral galaxy M81, suggesting that if the progenitor is a young NS, it must have been formed via an alternative pathway, such as the AIC of a WD, or the merger of compact stars in a binary system (Bhardwaj et al. 2021; Kirsten et al. 2021). Finally, the repeating FRBs 20190711A and 20201124A are observed to originate in typical star-forming galaxies at their respective redshifts (Heintz et al. 2020; Fong et al. 2021; Ravi et al. 2021).

In this paper, we introduce three additional bursts and their host galaxies to the existing sample and conduct a differential study of the host population of one-off and repeating FRBs using an updated sample of 16 FRB hosts (containing six repeating and 10 nonrepeating FRBs). The paper is laid out as follows: Section 2 presents the discovery of a new burst from the repeating FRB20180301A source (Luo et al. 2020) and resulting localization using the REALFAST system at the VLA. We also describe the radio and optical properties of the host galaxy of FRB20180301A. Section 3 presents the discovery and localization of two new (apparently) nonrepeating FRBs, namely FRB20191228A and FRB20200906A, found in the Commensal Real-time ASKAP Fast Transients (CRAFT) Survey (Macquart et al. 2010). We also describe the follow-up observations and identification of their host galaxies. In Section 4, we compare the overall population of FRB hosts with field galaxies at similar redshifts, based on the largest sample to date. In Section 5, we differentiate the hosts and compare the properties of the two subpopulations: repeating and one-off bursts. In Section 6, we compare the global properties and the projected physical offsets of FRBs to a range of both extragalactic transients and the projected source population of Galactic objects. Additionally, we compare the host-normalized offset distributions of FRBs with those of globular clusters associated with different galaxy types. We summarize our results in Section 7.

2. Localization of the Repeating FRB20180301A

2.1. Detection of a Repeating Burst

FRB20180301A, a burst originally detected in the Breakthrough Listen project at the Parkes radio telescope (Price et al. 2019), was observed to emit repeating radio pulses in sensitive follow-up observations with the Five-hundred-meter Aperture

²⁵ <http://frbhosts.org>

Spherical radio Telescope (FAST) telescope using the 19-beam receiver centered at 1.25 GHz (Luo et al. 2020). Fifteen repeating bursts, with fluences ranging from 0.03 to 0.4 Jy ms, were detected from the source of FRB20180301A in a total effective observation time of ~ 12 hr at FAST.

We performed follow-up observations of FRB20180301A using Director’s Discretionary Time (DDT) with 40 hr scheduled under VLA/19B-351, using the VLA in its C array configuration at the L band, spanning 1–2 GHz. We used the L16f5DC-realfast correlator mode, which enables a fast sampling time of 10 ms. We observed the field of FRB20180301A centered at RA(J2000): 06:12:54.96 and decl.(J2000): +04:38:43.60 covering a localization uncertainty region of at $2.6'$ at 1.25 GHz obtained from detection at FAST. The source was observed at nine epochs, each with an observation time of 2 hr in the period 2020 February–May. Each observation had an on-source time of ~ 1.5 hr and was searched for fast transients by the REALFAST system. The details of the REALFAST search procedure can be found in Law et al. (2018, 2020). We detected a repeat burst from FRB20180301A on 2020 May 28 at UTC 19:14:47.310 in the last epoch. It was detected in the real-time system with an image signal-to-noise ratio (S/N) of 10.8 at a DM of $517.45 \text{ pc cm}^{-3}$. The deep learning-based classifier *fetch* (Agarwal et al. 2020) reported an astrophysical probability of 99% for this burst. We used the recorded visibilities of the burst data to refine our estimate of the burst properties in an offline reprocessing. We reran the search with a finer DM grid at 0.1% fractional sensitivity loss on a subband of the data. This subband was manually identified to consist of burst signal. The refined search led to an improvement in detection significance to ~ 19 at a DM of 536 pc cm^{-3} . The top panel of Figure 1 shows the burst profile and dedispersed spectrogram. This figure also shows a weaker component ~ 50 ms after the burst that is present in the lower part of the band. This could either be a component of the main burst, or another burst from this FRB. We used the visibilities from the main component to determine the localization of this FRB.

We used BURSTFIT²⁶ (Aggarwal et al. 2021a) to model the spectro-temporal properties of FRB20180301A using its spectrogram. Following the method described in Aggarwal et al. (2021a), we modeled the spectrum and the pulse using a Gaussian, and fit for the following parameters simultaneously: arrival time of peak, Gaussian FWHM of pulse, peak of the spectrum, FWHM of the spectrum, fluence and DM. We used SCIPY.CURVE_FIT followed by Markov Chain Monte-Carlo methods to obtain the posterior distribution of all the fit parameters. The resulting burst properties are presented in Table 1.

2.1.1. Spatial Localization

The images generated by the REALFAST search pipeline make several assumptions (coarse DM grid, nonoptimal image size, simpler calibration algorithm, etc.) during calibration and imaging. To address these, we used the raw, dedispersed burst visibilities to form the burst image using CASA (McMullin et al. 2007). We ran the full CASA pipeline to generate VLA calibration tables for this observation. We then used the CASA task *applycal* to apply those calibration and flagging tables to the burst data. Observations of calibrator 3C 147 were used to calibrate the flux density scale, band-pass, and delays. The

nearby source J0632+1022 was used to calibrate the complex gain fluctuations over time, by observing it every 20 minutes. We then used CASA tasks *tclean* and *imfit* to generate a radio image and fit an ellipse to the burst position. The initial burst position was found to be R.A.(J2000): $06^{\text{h}}12^{\text{m}}54^{\text{s}}.47$ and decl.(J2000): $+04^{\circ}40'15''.6$ with a statistical uncertainty of $0''.01$ in R.A. and $0''.01$ in decl. (see bottom panel of Figure 1).

2.1.2. VLA Radio Continuum Image

In addition to the fast-sampled data with an integration time on the order of a few milliseconds generated by REALFAST, the VLA correlator creates slow-sampled data with an integration time of 5 s. This slow-sampled data will average out any fast-varying signal (like FRBs) but is suitable for finding any persistent radio source near the burst location. We made separate images for each epoch and combined images to search for any persistent or slowly varying emission from the FRB location.

The slow-sampled data was calibrated using the standard VLA calibration pipeline, followed by manual data inspection and further flagging. We used *tclean* to produce images. Manual flagging of the data set was done to allow for much finer and in-depth radio frequency interference flagging than autoflagging algorithms. The inputs of *tclean* used the gridding *wproject* with 128 *wprojplanes*. The deconvolver was set to *mtmfs* and Briggs weighting was used with a robustness parameter of 0. These parameters were chosen to help reduce noise from sources outside the primary beam as well as suppressing minor baseline-dependent errors. The full field of view was also imaged to allow cleaning on these bright sources, specifically sources $\sim 42'$ and $\sim 30'$ away from the phase center.

Once *tclean* was run, the rms near the center of the primary beam was found to be in the range $23\text{--}26 \mu\text{Jy beam}^{-1}$ for all epochs. The image rms is consistent with the combined effect of confusion noise ($18 \mu\text{Jy beam}^{-1}$) and thermal noise ($16 \mu\text{Jy beam}^{-1}$ in each epoch). Combining the first four epochs and last four epochs produces images with rms of $21 \mu\text{Jy beam}^{-1}$, consistent with reduced thermal noise added to a fixed confusion noise. We find no persistent radio source above a 3σ flux density of $63 \mu\text{Jy beam}^{-1}$, yielding a luminosity limit of $1.8 \times 10^{22} \text{ W Hz}^{-1}$ at 1.5 GHz.

2.1.3. Astrometry

We tested our astrometric precision by associating radio sources in the FRB-epoch VLA image with the Karl G. Jansky Very Large Array Sky Survey (VLASS; Lacy et al. 2020) Epoch 1 Quick Look catalog (Gordon et al. 2020). We reimaged the FRB epoch, selecting an interval of 30 s centered on the FRB for investigating astrometric accuracy. We ran the PYSE source-finding package (Spreeuw et al. 2018) on this 30 s image and identified six radio sources above a significance level of 15σ . All these sources had VLASS counterparts within a $2''$ search radius. We measured the weighted mean and associated uncertainty of the offsets between these six sources in the 30 s snapshot image and their VLASS catalog positions, measuring $156 \pm 330 \text{ mas}$ and $-197 \pm 223 \text{ mas}$ in R.A. and decl. respectively. However, the scatter in the measured offsets is clearly not due solely to the statistical (signal-to-noise limited) measurement uncertainty, with the χ^2 of the weighted mean fit being 50.40 for 10 degrees of freedom. This is not

²⁶ <https://github.com/thepetabyteproject/burstfit>

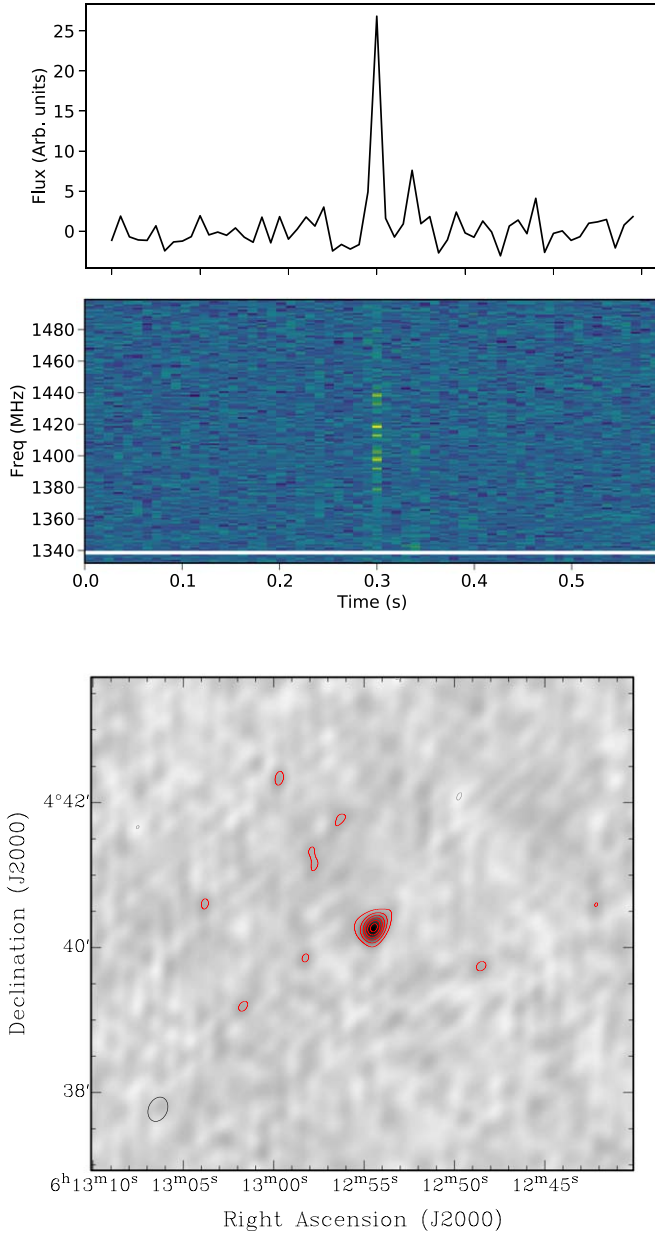


Figure 1. REALFAST detection of FRB20180301A. Top and middle panels show the dispersion-corrected frequency-integrated profile and spectrum of FRB20180301A. Bottom panel shows the fast-sampled (10 ms) calibrated radio image of FRB20180301A. The red contour levels are placed at $11.2 \text{ mJy beam}^{-1}$ times factors of $[-3, 3, 6, 9, 12, 15, 18]$. The synthesized beam in the burst image is $20''.9 \times 15''.5$ at a position angle of $-24^\circ 1$.

unexpected, given the potential for systematic differences in centroid position due to, e.g., the different frequency and resolution of our 30 s image versus the VLASS catalog. Previous studies using ASKAP (Day et al. 2021) have examined a large number of fields to estimate a scaling factor that can be applied to the weighted mean uncertainty to correct (on average) for these contributions, but the value of the scaling factor should depend on the telescope and reference catalogs used. Here, we instead take an unweighted mean of the six source offsets, which effectively assumes that the signal-to-noise limited contribution to each measured offset is small, and yields a more conservative estimation of the mean offset and uncertainty of $556 \pm 619 \text{ mas}$ and $-297 \pm 603 \text{ mas}$ in R.A. and decl., respectively. We note that the astrometric accuracy of the

VLASS Epoch 1 is well characterized, with a mean offset of the order $0''.0$ in R.A. and $0''.15$ in decl.²⁷ We corrected for this positional offset in the reference VLASS positions, and obtain a final offset correction of $0''.75$ in R.A. and $-0''.30$ in decl. The final position of FRB20180301A after correcting for positional offsets along with the statistical and systematic uncertainties is R.A.(J2000): $06^{\text{h}}12^{\text{m}}54^{\text{s}}.44(\pm 0''.01 \pm 0''.62)$ and decl.(J2000): $+04^{\text{d}}40'15.8(\pm 0''.01 \pm 0''.6)$. These are also listed in Table 1.

We conducted additional tests on the FRB-epoch data to investigate the astrometric stability on \sim minute scales across the entire observation duration, generating a set of images with a spacing of 3 minutes. The mean offset varied by up to half an arcsecond between adjacent 3 minutes images, consistent with our previous experience of *L*-band observations and implying a potential gradient in the observed positional offsets of up to $\sim 0''.2 \text{ minute}^{-1}$. We noted, however, that the average offset derived from the 30 s image centered on FRB does not lie on an interpolation between those derived from adjacent 3 minutes images, suggesting some structure on $\ll 3$ minutes timescales. We note that any remaining variability on < 30 s timescales could lead to a small, uncorrected positional bias.

2.1.4. Optical Follow-up

In archival Panoramic Survey Telescope and Rapid Response System (Pan-STARRS) images we identify a faint galaxy, PSO J093.2268+04.6703, as the putative host of FRB20180301A. We acquired deep (0.5–0.7 hr in each band) follow-up imaging of the FRB field with the Nordic Optical Telescope (NOT) using the Sloan filters *u*, *g*, *r*, *i*, and *z* on nights between UT 2021 October 26 and December 14, followed by additional deep ($36 \times 100 \text{ s}$) Gemini *r*-band observations on UT 2021 January 25. The Gemini image was astrometrically calibrated to match the Gaia DR2 catalog (Gaia Collaboration et al. 2018; Lindegren et al. 2018), with a relative accuracy of $0''.2$. We note that there is an additional nearby source to the south of the identified host galaxy in the field of FRB20180301A. The morphology of this source is consistent with being point-like, so we classify it as a Galactic foreground star.

Observations of the host with the Keck/DEep Imaging Multi-Object Spectrograph (DEIMOS) on UT 2020 September 17 determined the galaxy’s redshift $z = 0.3304$ based on nebular emission lines such as $[\text{N II}]$ and $\text{H}\alpha$. The measured redshift was found to be consistent with the redshift range ($z = 0.13\text{--}0.35$) estimated by extragalactic DM in Luo et al. (2020). We also performed near-IR (NIR) observations of the galaxy in the *JHK* bands using the MMT telescope on UT 2021 February 27 and 28. The photometric measurements derived from MMT imaging, along with those from NOT, were used by CIGALE (Noll et al. 2009) for spectral energy distribution (SED) fitting to estimate the stellar mass of the galaxy (see the Appendix for details). The deep *r*-band Gemini imaging was used for the probabilistic host galaxy association analysis. We find a probabilistic association of transients to their hosts (PATH; Aggarwal et al. 2021b) probability of 99.9% for the association of FRB20180301A with the given galaxy. The host is presented in Figure 2 and properties are listed in Table 1.

²⁷ https://library.nrao.edu/public/memos/vla/vlass/VLASS_013.pdf

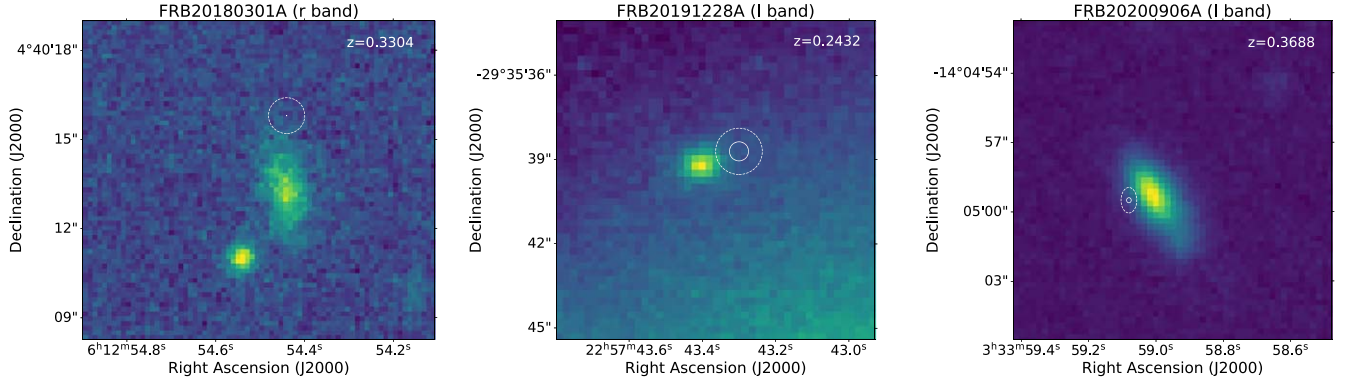


Figure 2. *r*-band Gemini image of the host of repeating FRB20180301A and *I*-band FORS2 images of the hosts of FRB20191228A and FRB20200906A, overplotted with the positions of each FRB. The white solid and dashed circle/ellipse represent the 1σ statistical and systematic uncertainty, respectively, in the FRB position.

Table 1
Measured and Derived Properties of the New FRBs Presented in This Work

Properties	FRB20180301A	FRB20191228A	FRB20200906A
Arrival time ^a (UT)	2020-05-28 19:14:47.310	2019-12-28 09:16:16.444	2020-09-06 21:40:50.923
S/N	19.0 ^b	22.9	19.2
DM (pc cm ⁻³)	536 ⁺⁸ ₋₁₃	297.5 ± 0.05	577.8 ± 0.02
DM _{ISM} NE2001 (pc cm ⁻³)	152	33	36
DM _{ISM} YMW16 (pc cm ⁻³)	254	20	38
DM _{cosmic} ^c (pc cm ⁻³)	289	210	324
R.A. (J2000)	06 ^h 12 ^m 54 ^s .44(±0 ^{''} .01 ± 0 ^{''} .62)	22 ^h 57 ^m 43 ^s .30(±0 ^{''} .34 ± 0 ^{''} .83)	03 ^h 33 ^m 59 ^s .08(±0 ^{''} .10 ± 0 ^{''} .34)
Decl. (J2000)	+04 ^d 40 ['] 15.8(±0 ^{''} .01 ± 0 ^{''} .6)	-29 ^d 35 ['] 38.7(±0 ^{''} .3 ± 0 ^{''} .8)	-14 ^d 04 ['] 59.5(±0 ^{''} .1 ± 0 ^{''} .6)
Fluence (Jy ms)	4.9 ^{+0.5} _{-0.4}	40 ⁺¹⁰⁰ ₋₄₀	59 ⁺²⁵ ₋₁₀
Pulse width (ms)	7 ⁺² ₋₃	2.3 ± 0.6 ^d	6.0 ± 0.6
Spectral energy density ^e (erg Hz ⁻¹)	6.9 × 10 ³⁰	6.4 × 10 ³¹	1.1 × 10 ³²
Persistent source, radio luminosity (W Hz ⁻¹)	<1.8 × 10 ²² 1.5 GHz	<3.4 × 10 ²¹ 6.5 GHz	<4.3 × 10 ²¹ 6 GHz
Host galaxy			
Redshift ^f	0.3304	0.2432	0.3688
<i>u</i> - <i>r</i> ^g (rest-frame)	0.90 ± 0.11	2.13 ± 0.74	1.22 ± 0.11
<i>M_r</i> ^g (rest-frame)	-20.18 ± 0.07	-18.26 ± 0.05	-21.49 ± 0.05
Galactic <i>E</i> (<i>B</i> - <i>V</i>) ^g	0.46	0.02	0.05
<i>M_*</i> ^g (10 ¹⁰ <i>M_⊙</i>)	0.23 ± 0.06	0.54 ± 0.60	1.33 ± 0.37
SFR ^f (<i>M_⊙</i> yr ⁻¹)	1.93 ± 0.58	0.50 ± 0.15	0.48 ± 0.14
log(sSFR) (yr ⁻¹)	-9.08	-10.03	-10.44
Metallicity ^{f,h}	8.70	8.48	8.76
Projected offset from galaxy center (kpc)	10.8 ± 3.0	5.7 ± 3.3	5.9 ± 2.0
Effective radius (kpc)	5.80 ± 0.20	1.78 ± 0.06	7.58 ± 0.06

Notes. 1σ uncertainties are quoted for these measurements.

^a Arrival time of a repeating burst from FRB20180301A source and one-off ASKAP/CRAFT FRBs.

^b This is the coherent S/N of the FRB detected in the VLA image.

^c Estimated using the Macquart relation.

^d FRB20191228A shows a scattering tail of 6.1(6) ms. The deconvolved width is 2.3(6) ms.

^e The energies are derived assuming a flat spectrum for FRBs ($\alpha = 0$) and zero *k*-correction.

^f These measurements are derived from spectroscopy.

^g These properties are derived using CIGALE SED fitting.

^h In units of $12 + \log[\text{O}/\text{H}]$.

3. ASKAP Localization of Apparently Nonrepeating FRBs

Here we report the discoveries of the single bursts from two new FRB sources, FRBs 20191228A and 20200906A, discovered in the CRAFT incoherent-summed (ICS) searches with ASKAP (Bannister et al. 2019a). The burst pulse profiles and dynamic spectra are shown in Figure 3.

3.1. FRB20191228A

FRB20191228A was detected on 2019 December 28 at UTC 09:16:16.44440 during CRAFT observations conducted with ASKAP, with 28 antennas in a 336 MHz band centered on 1271.5 MHz. The burst had a detection S/N of 23 at a DM = 297.5(5) pc cm⁻³. The real-time detection in online

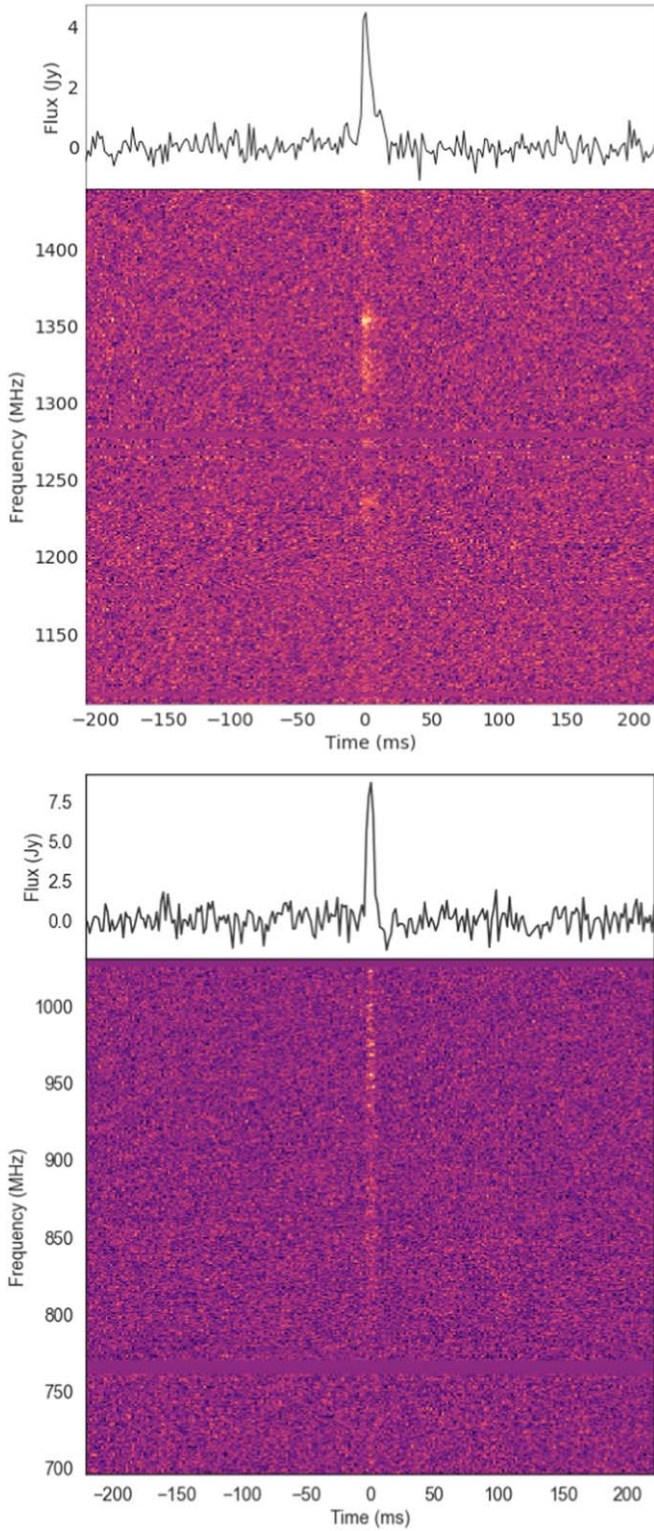


Figure 3. Pulse profile and dynamic spectra for FRB20191228A (top) and FRB20200906A (bottom). FRB signals are dedispersed at the S/N maximized DM of 297.5 pc cm^{-3} and 577.8 pc cm^{-3} for FRB20191228A and FRB20200906A, respectively.

incoherent-sum data triggered a download of 3.1 s of voltages around the FRB. The offline correlation of voltages across 28 antennas and their interferometric analysis led to an initial localization of FRB20191228A.

On 2020 January 31, we used the Australia Telescope Compact Array (ATCA) in the frequency range of 1.1–3.1 GHz to perform astrometric observations of background sources near the position of FRB20191228A, to refine the position of the burst. In addition to four target background sources in the field of FRB20191228A (J2258–2929, J2255–2937, J2258–2955, and J2259–2957), we observed three gain calibrators (PKS2254–367, PKS2337–334, and PKS2255–282). For each target background source, we obtained three position estimates—one for each gain calibrator—by applying phase-calibration solutions derived from that calibrator. We observed a scatter of $\sim 80 \text{ mas}$ in R.A. and $\sim 200 \text{ mas}$ in decl. in the position of the background sources depending on which gain calibrator was used. To account for this systematic uncertainty to the ATCA positions, for each background source we took a weighted mean of the three positions to estimate the probable location, and added the average residual offset from this mean position in quadrature to our estimate of the absolute positional uncertainty for the source.

The positions of target sources obtained from the ATCA radio image were compared with those obtained from the 3.1 s ASKAP data, following the method described in Day et al. (2020), to astrometrically register the FRB image frame to that of the International Celestial Reference Frame (ICRF3; Gordon 2018) and estimate the accuracy of this registration. J2258–2929 and J2259–2957 were excluded from the field source comparison due to low S/N in the ASKAP image for the latter, and the former being resolved.

Finally, we computed a weighted mean systematic image frame offset using the method described in Day et al. (2021). We found positional offsets of $0''.410 \pm 0''.830$ and $-0''.856 \pm 0''.823$ in R.A. and decl., respectively. After accounting for astrometric shifts in the image frame as well as statistical and systematic errors, the final FRB position is R.A.(J2000): $22^{\text{h}}57^{\text{m}}43^{\text{s}}.30(\pm 0''.34 \pm 0''.83)$ and decl.(J2000): $-29^{\circ}35'38.7(\pm 0''.3 \pm 0''.8)$.

3.1.1. Follow-up Observations

The burst position is $1/8$ from the first-magnitude star Fomalhaut ($\alpha \text{ PsA}$), which severely complicated identification and characterization of the optical counterpart.

Deep imaging with the FORS2 instrument at the European Southern Observatory’s (ESO) Very Large Telescope (VLT) was performed in the g band ($5 \times 90 \text{ s}$) and I band ($20 \times 100 \text{ s}$) on UT 2020 September 21, while using the movable slitlets normally employed for multiobject spectroscopy to completely mask the lower of the two CCDs to protect the detector from saturation by Fomalhaut. The seeing ranged between $0''.6$ and $0''.9$ during the observations.

The individual frames were bias subtracted and flatfielded using the ESOReflex package (Freudling et al. 2013). To overcome the glare produced by Fomalhaut, a 2D polynomial was fit to a patch of sky centered on the burst position in each individual frame, after masking sources. This model was then subtracted from the patch. The glare-subtracted images were coadded with the Montage package (Berriman & Good 2017). A candidate host galaxy was identified with centroid approximately $1''.5$ from the burst coordinates with a 100% PATH association probability (see Figure 2). Photometry of the identified galaxy was performed with Source-Extractor (Bertin & Arnouts 1996) using a circular aperture with a $5''$

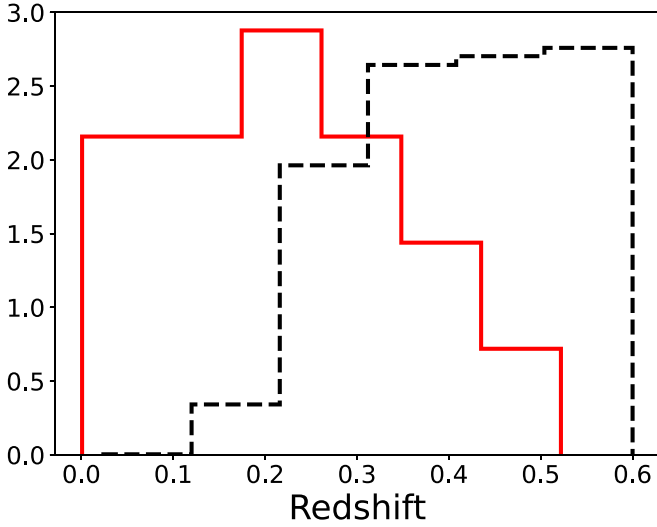


Figure 4. Redshift distribution of the FRB hosts (red) and PRIMUS sample of field galaxies (dashed black) where the area under the histogram integrates to 1. The PRIMUS sample lacks good stellar mass and SFR measurements of field galaxies for $z < 0.2$.

diameter. The effect of the glare subtraction on the photometry was investigated, and the uncertainty introduced by the procedure quantified, using injected synthetic sources of known magnitude (making use of *Astropy*; Robitaille et al. 2013).

On UT 2020 November 8, the Keck/Low Resolution Imaging Spectrometer (LRIS) spectrograph was used to perform spectroscopic observations in order to determine the galaxy redshift. The nebular emissions such as H α , [O III] established the redshift of the host to be $z = 0.243$.

We also performed observations of the host of FRB20191228A using the ATCA at center frequencies of 5.5 and 7.5 GHz to search for a compact and persistent radio emission. We did not detect any radio emission above $22 \mu\text{Jy beam}^{-1}$ (3σ) constraining the luminosity of the source to be $< 3.4 \times 10^{21} \text{ W Hz}^{-1}$ at 6.5 GHz.

3.2. FRB20200906A

FRB20200906A was discovered in the incoherent sum of seven ASKAP antennas on UTC 2020 September 6 21:40:50.923 during CRAFT observations at 864.5 MHz. The burst had an optimal S/N of 19.2 at a DM of $577.8(2) \text{ pc cm}^{-3}$ in the low-time-resolution search data stream. Voltages spanning 3.1 s around the FRB were downloaded, cross-correlated and imaged offline to obtain a preliminary position of the burst. The astrometric registration was performed by comparing background sources in the 3.1 s ASKAP image with their NRAO VLA Sky Survey (NVSS) radio source catalog (Condon et al. 1998) counterparts. We cross-matched seven sources and computed a weighted mean systematic image frame offset using the method described in Day et al. (2021). We found positional offsets of $2''.05 \pm 0''.34$ and $0''.51 \pm 0''.55$ in R.A. and decl., respectively. The final burst position after correcting for the astrometric shifts in the image frame is R.A.(J2000): $03^{\text{h}}33^{\text{m}}59^{\text{s}}08(\pm 0''.10 \pm 0''.34)$ and decl.(J2000): $-14^{\circ}04'59.5(\pm 0''.1 \pm 0''.6)$, where statistical and systematic uncertainties in R.A. and decl. are quoted respectively.

3.2.1. Follow-up Observations

A candidate host galaxy for FRB20200906A was identified in the DES, Pan-STARRS and AllWISE database as DES J033358.99–140459.2, PSO J033358.994–140459.287, and J033358.99–140459.1, respectively, with 100% PATH association probability (see Figure 2). On UT 2020 December 20 and 22, we performed follow-up observations using VLT/FORS2 in the g and I bands following a similar strategy as for FRB20191228A (Section 3.1.1) but without the need to mask the lower CCD. On UT 2020 September 17, we also triggered Keck/DEIMOS for spectroscopic observations, and found the redshift of the putative host to be $z = 0.3688$. The photometric measurements from Pan-STARRS and those from the VLT were used to model the SED of the host galaxy. The derived properties are presented in Table 1.

We triggered the VLA (project code: VLA/20A-157) on UT 2020 September 22 to observe the host galaxy of FRB20200906A in the 4–8 GHz frequency range. We found no radio emission from the host galaxy above a 3σ flux density of $12 \mu\text{Jy beam}^{-1}$, implying an upper limit on the source’s luminosity to be $< 4.3 \times 10^{21} \text{ W Hz}^{-1}$ at 6 GHz.

4. Comparing FRB Host Galaxies to the Underlying Field Galaxy Population

In this section, we place the overall population of FRB hosts in context with the field galaxy population, expanding on our earlier work (Bhandari et al. 2020; Heintz et al. 2020).

4.1. Sample Selection

We use the data published in Heintz et al. (2020) and Mannings et al. (2020), and measurements derived for the hosts in this work. We also update the measurements published for a subset of FRB hosts (see the Appendix). For FRB20171020A, FRB20201124A, and FRB20200120E, we use the data published in Mahony et al. (2018), Fong et al. (2021), and Bhardwaj et al. (2021), respectively (see Table A1 and A3).

We considered only the FRB host galaxies for which the PATH posterior probability is greater than 90% (see last column of Table A2). This includes all three of the new FRBs presented here which have posterior probability $P(O|x) > 0.999$. The hosts of FRB20190614D (Law et al. 2020), FRB20181112A (Prochaska et al. 2019), and FRB20190523A (Ravi et al. 2019) have low probabilities of $P(O|x)$ of 0.58, 0.67, and 0.82, respectively, and are therefore excluded. Also, FRB20191001A has two nearby candidate hosts at a common redshift (Bhandari et al. 2020) that yield PATH posterior probabilities $P(O|x) = 0.6$ and 0.4 . We proceeded by adopting the galaxy with smaller angular separation from the FRB as the host, which is akin to adopting a stronger prior on the projected offset than adopted by Aggarwal et al. (2021b). Future associations will refine this assumption. We also included the host of FRB20200120E (Bhardwaj et al. 2021; Kirsten et al. 2021) and the candidate host for FRB20171020A, because of their low probability of chance association (F. North-Hickey et al. 2021, in preparation). Thus, we obtained a sample of 16 confident host associations for our analysis, of which 10 are hosts of apparently nonrepeating FRBs and six host repeating FRBs (see Table A3).

The spectroscopy and photometry of all FRB hosts are analyzed with the *pPXF* (Cappellari 2017) and *CIGALE*

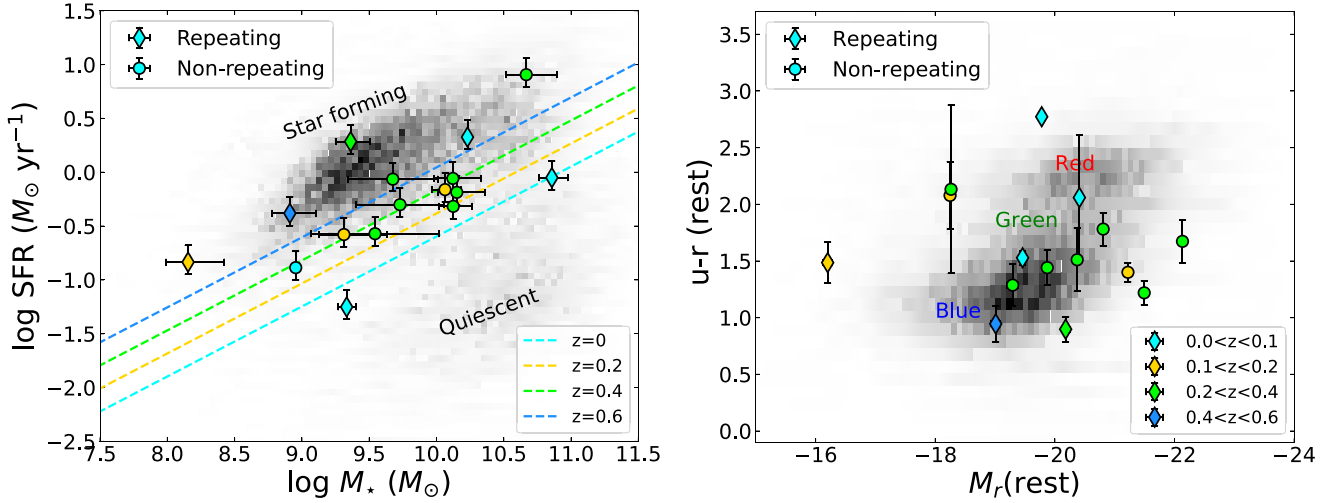


Figure 5. Left: star formation rate and stellar mass distributions of the host galaxies of six repeating and 10 one-off FRBs compared against a population of galaxies at $z < 0.6$ taken from the PRIMUS survey (Moustakas et al. 2013). Diamond and circle symbols represent the hosts of repeating and nonrepeating FRBs, respectively. The boundary separating the star-forming and quiescent galaxies and its evolution with redshift (Moustakas et al. 2013) is presented by colored dashed lines. Right: rest-frame color–magnitude diagram of the host galaxies of a sample of six repeating and nine one-off FRBs compared to the population of PRIMUS galaxies at $z < 0.6$. FRB20171020A is not included due to lack of $u - r$ measurement. We also note that the observed magnitudes for FRB20201124A and FRB20200120E are approximated as rest-frame magnitudes because of their low redshifts and, thus, small k -correction. For both plots, the FRB host data is color coded and divided into four redshift bins of $<0.0 < z < 0.1$ (cyan), $<0.1 < z < 0.2$ (yellow), $<0.2 < z < 0.4$ (green), and $<0.4 < z < 0.6$ (blue).

(Noll et al. 2009) software packages by fitting a set of stellar population models and star formation history to the spectra and SED, respectively (see Heintz et al. (2020) for details). The star formation rates (SFRs) are derived from the dust-corrected $H\alpha$ line flux measurements (Kennicutt 1998), adopting an initial mass function (IMF) from Chabrier (2003).

We used the PRISM Multi-object Survey (PRIMUS) data as an underlying sample of field galaxies (Moustakas et al. 2013). We restricted the redshift range to be $z < 0.6$ to match the redshifts of the FRB hosts (see Figure 4). We used a K -correct synthesized rest-frame SDSS absolute magnitude of $\sim 108,000$ galaxies and stellar masses/SFRs of $\sim 31,200$ galaxies. We note that the PRIMUS sample lacks good stellar mass and SFR measurements of field galaxies for $z < 0.2$. All stellar masses and SFRs assume a universal (Chabrier 2003) IMF and are derived using the SED-modeling code *iSEDfit*, designed to extract the physical properties of galaxies (Moustakas et al. 2013).

4.2. Comparison with Underlying Population

Figure 5 shows our comparison of the color–magnitude and SFR– M_{*} distributions of the FRB host galaxies with those of the general population of galaxies at redshift < 0.6 . The left panel of Figure 5 presents the current SFR as a function of M_{*} . The hosts of repeating and one-off bursts are distinguished by symbol shape, and the color represents the four redshift bins. We also present the redshift evolution of the boundary separating the star-forming and quiescent galaxies (Moustakas et al. 2013). Most of the FRB hosts lie in or around the star-forming cloud of galaxies, but are offset from the star-forming main sequence for galaxies with similar stellar masses. We caution here that since a significant fraction of the FRB hosts show low-ionization nuclear emission-line region (LINER)-like emission (see Section 4.4), the derived SFR should in these cases only be considered as upper limits since the total line emission may not reflect solely that of star formation. This

would further offset the FRB hosts from the star-forming main sequence.

The right panel of Figure 5 shows a color–magnitude diagram and provides information about the overall stellar populations in these galaxies. The late-type galaxies with ongoing star formation and, therefore, young stellar populations lie in the “blue cloud”, i.e., blue galaxies (Strateva et al. 2001), while massive early-type galaxies live in the “red and dead” zone characterized by very low star formation and hence older stellar populations, i.e., red galaxies. The host galaxies of the FRBs appear to lie on the luminous side of the absolute magnitude distribution, mainly near the “blue cloud” and “green valley” region, where galaxies are expected to be transitioning between star-forming and quiescent systems (Martin et al. 2007). We observe a dearth of red galaxies in our current sample of FRB host galaxies.

4.3. Do FRB Hosts Track Stellar Mass and Star Formation Rates?

In Figure 6 we again present the color–magnitude diagram, but with the background PRIMUS galaxy sample weighted by their stellar masses and divided into redshift bins of $0.0 < z < 0.3$ and $0.3 < z < 0.6$. This is a good approximation of where most stars are in the local universe. We show that the majority of FRB hosts do not trace massive red galaxies and also do not seem to align with the color–magnitude diagram space of the peak of stellar mass-weighted blue galaxies which tend to redder color, particularly for the low-redshift bin. To quantify this trend, we examined the null hypothesis that FRB hosts (both repeating and nonrepeating population) track stellar mass. The galaxy stellar mass function (GSMF) of low- z galaxies, $\Phi(M_{*})\Delta M$, was weighted by stellar mass and compared to the observed FRB host mass distribution. We used the double Schechter function to model GSMF for all, star-forming, and passive galaxies in the redshift range $0.2 < z < 0.5$ in the COSMOS field (Davidzon et al. 2017). Our Kolmogorov–Smirnov (KS) tests comparing the

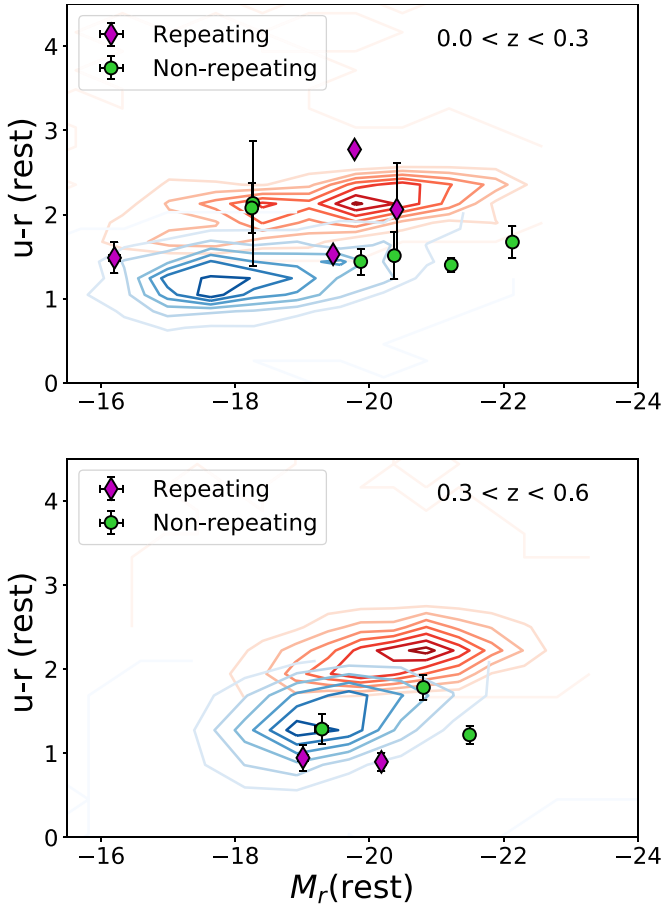


Figure 6. Approximation of the stellar density in blue and red galaxies as presented by blue and red contours, respectively, and derived from the PRIMUS galaxies in the color–magnitude diagram for the two redshift bins. The shading from white to respective color represent outer to inner contour levels. The contour levels are set the same for blue and red galaxies. The bright red region shows that most of the stars in the local universe are concentrated in massive red galaxies. Green and magenta data points are the sample of one-off and repeating FRB hosts, respectively. We observe that FRBs are distributed in normal blue galaxies.

Table 2

P-values for Two-sample 1D KS for Comparing the Mass-weighted Stellar Mass Distributions (of All, Star-forming (SF), and Quiescent (Q) Samples), Star Formation Rate Volume Density Distribution and the Double Exponential Function for sSFRs of Field Galaxies with FRB Host (Repeating and Nonrepeating) Cumulative Mass, SFR, and sSFR Distribution

FRB Type	Stellar Mass			SFR All	sSFR SF
	All	SF	Q		
All	4e-6	0.002	4e-11	4e-4	5e-6
Rep.	0.014	0.029	6e-4	0.056	0.037
Nonrep.	7e-5	0.005	4e-8	0.001	7e-6

cumulative mass distributions of all FRB hosts, together and separately for the two FRB populations, with the mass-weighted stellar mass distribution of field galaxies yield a *p*-value $P_{\text{KS}} < 0.05$ (see Table 2). Therefore, we reject the null hypothesis that FRB hosts directly track stellar mass with more than 95% confidence, consistent with the findings of Heintz et al. (2020). We note that the redshift range of FRB hosts is broader than the range used for the stellar mass-weighted mass function. We replicated the above analysis using a subset of FRBs in the range $0.2 < z < 0.5$ to investigate if the differences

in the redshift had an effect on our conclusions. We obtained identical results, indicating that the effect of redshift evolution is not substantial.

Furthermore, we tested the null hypothesis that FRB hosts track SFRs. We used the star formation rate distribution function derived from the UV and IR luminosity Schechter functions for the local universe using Galaxy Evolution Explorer (GALEX; Bothwell et al. 2011) data. We then computed the star formation rate volume density distribution function, which is given by $\Phi(\Psi) \times \Psi$, where Ψ is the star formation rate in $M_{\odot} \text{ yr}^{-1}$. The *p*-values for the KS test performed between the cumulative star formation rate volume density distribution function and the SFRs of FRB hosts (both repeating and nonrepeating population) in our sample are presented in Table 2. We find the *p*-values for all and nonrepeating subset to be $< 10^{-3}$. (Considering the SFRs as upper limits due to possible LINER emission contamination (see Section 4.4) would make the discrepancy even more significant.) However, when comparing with the repeating host population, we find a *p*-value slightly higher than our significance level. As a result, while we reject the null hypothesis with greater than 95% confidence for all FRB hosts, we are unable to reject it with the same level of confidence for the repeating host population. We note a possible caveat of comparing the SFRs derived using the UV and IR luminosity for the GALEX sample with those derived using H α emission-line luminosity for the FRB host sample. Nevertheless, Lee et al. (2009) showed a coarse agreement between the far-UV and H α SFRs, where the SFRs agree to within about a factor of two for the majority of galaxies with $\text{SFR} \geq 0.01 M_{\odot} \text{ yr}^{-1}$.

Finally, we investigated the specific star formation rates (sSFRs) of FRB hosts in our sample with those of sSFR functions derived from the star-forming sample of galaxies defined by a main sequence using a color–color selection in the COSMOS and GOODS surveys in the redshift range 0.2–0.4 (Ilbert et al. 2015). The sSFR function can be modeled as a log-normal or a double exponential profile for a given stellar mass bin range (Equations (2) and (3) of Ilbert et al. 2015). We computed the function over four mass bins ranging from $9.5 < \log(M) < 11.5$ and combined them together. The weighted cumulative sum of this sSFR function is compared to the cumulative distribution of sSFRs of FRB hosts in the same mass range. The results are presented in Table 2 and cumulative distributions are presented in Figure 7. We observed that FRB hosts do not follow the sSFRs of star-forming galaxies and thus reject the null hypothesis with more than 95% confidence.

Thus, we conclude that FRB hosts have lower M_{*} , SFR, and sSFR than randomly selected field galaxies weighted by M_{*} , SFR, or sSFR.

4.4. Baldwin–Phillips–Terlevich Diagram

To identify the dominant source of ionization in FRB host galaxies, we plot their nebular emission-line ratios, namely [N II]/H α and [O III]/H β , in a Baldwin–Phillips–Terlevich (BPT) diagram (Baldwin et al. 1981) in Figure 8. This diagram can also be used to distinguish between star-forming (SF) galaxies, LINER galaxies, and active galactic nuclei (AGNs; see Kewley et al. 2001 for more details). For comparison, we show the distribution of nearby ($0.02 < z < 0.4$) emission-line ($> 5\sigma$ significance) galaxies from the Sloan Digital Sky Survey

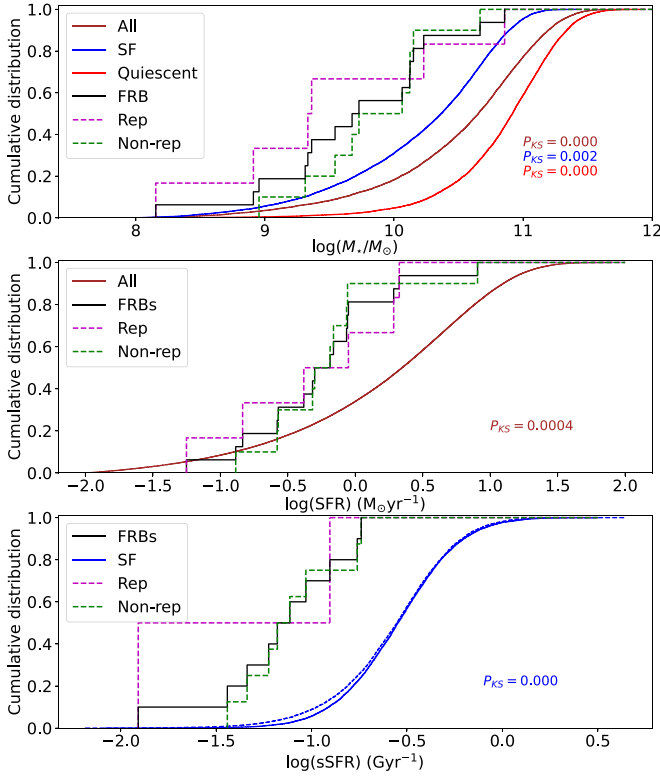


Figure 7. Top: comparison of FRB cumulative mass distribution with mass-weighted stellar mass distribution for all field galaxies (brown), star-forming galaxies (blue) and quiescent galaxies (red). Middle: comparison of FRB host cumulative SFR distributions (black) with the star formation rate volume density distribution function for all field galaxies in the local universe (brown). Bottom: comparison of sSFRs for FRBs in the mass range $9.5 < \log(M) < 11.5$ with the log-normal (solid) and double exponential functions (dashed) for sSFRs of main-sequence star-forming galaxies.

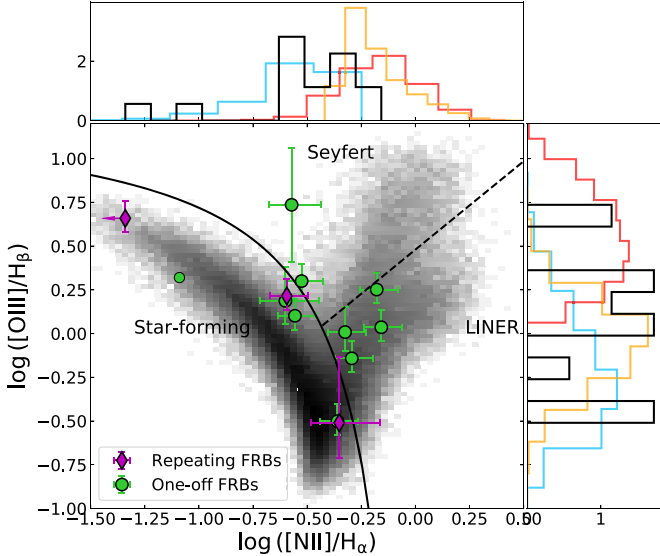


Figure 8. BPT classification diagram for FRB hosts. The gray-scale background shows the density distribution of SDSS galaxies with redshifts $0.02 < z < 0.4$. The dashed and dotted black lines represent the demarcation line between SF galaxies and AGNs (Kauffmann et al. 2003), and AGN and LINERs (Cid Fernandes et al. 2010), respectively. The majority of FRB hosts are SF and LINER galaxies. Top and sideways inset present the histograms of the ratio of $[NII]/H\alpha$ and $[OIII]/H\beta$, respectively, for FRBs (black), AGNs (red), SF (light blue), and LINER (orange) galaxies. We note that a smaller sample of FRBs is shown in this plot, due to either lack of available spectral line data or the nondetection of required emission lines.

(SDSS) including the standard demarcation lines between SF, AGN, and LINER galaxies (Kauffmann et al. 2003; Cid Fernandes et al. 2010). We performed a 2D KS test to compare the host population of FRBs with that of underlying SF, AGN, and LINER galaxies, and found that they are not drawn from a specific class ($P_{KS} < 10^{-3}$), which remains consistent with the findings of Heintz et al. (2020). The majority of FRB hosts occupy the star-forming and LINER region of the BPT diagram. We note that all three hosts of repeating FRBs lie in the star-forming region, and the host of repeating FRB20121102A remains an outlier as compared to the hosts of other FRBs (Li et al. 2019).

5. Disentangling the Host Galaxies of Repeating and Nonrepeating FRBs

The progenitors of FRBs are linked to the specific stellar population and environments of their host galaxies. Based on the larger set of FRBs and their hosts presented here, in combination with previous literature identifications, we leverage this larger sample to further constrain the likely progenitor channels of FRBs. More specifically, we aim to quantify whether the repeating and apparently nonrepeating bursts are hosted by distinct galaxy environments. This might provide further clues to whether their progenitor channels are physically distinct.

Initially, Heintz et al. (2020) found that FRB hosts seem to show an overall broad, continuous range of physical properties. They noted that the hosts of repeating FRBs generally occupied the faint, low-mass end of the FRB galaxy distribution. Here, we performed a differential analysis of the properties of the larger sample of FRB hosts. In Figure 9 we compared the projected physical offsets, SFRs, stellar masses, metallicities, r -band luminosities and sSFRs of repeating and nonrepeating FRB host populations. We found the KS test p -values to be greater than our threshold statistical significance level ($\alpha = 0.05$). Thus, the null hypothesis that these distributions are drawn from the same underlying distribution cannot be rejected. The present sample of FRB hosts thus do not indicate strong physical distinctions between the two apparent source populations.

6. Comparison of the FRB Host Galaxy Properties with other Transients

6.1. Extragalactic Transients

Studies of extragalactic transients often use their physical offsets from the center of their hosts, and locations within their host galaxies, to aid in inferring the nature of their progenitors. In the past, such investigations including other global properties for a small sample of FRB hosts have been conducted (Bhandari et al. 2020; Heintz et al. 2020; Li & Zhang 2020; Mannings et al. 2020; Safarzadeh et al. 2020; Bochenek et al. 2021). The majority of them suggest that galaxies hosting gamma-ray bursts (SGRBs) and CCSNe are similar to galaxies hosting FRBs. Additionally, the progenitor scenarios of LGRBs and SLSNe have been disfavored for the majority of FRBs. Recently, ultra-luminous X-ray sources (ULX)-like binaries were proposed as a possible progenitor for periodically active FRBs (Sridhar et al. 2021). Motivated by such studies, we performed two-sample 1D KS tests comparing the distributions of various global host properties of the most updated sample of FRBs together and separated into two

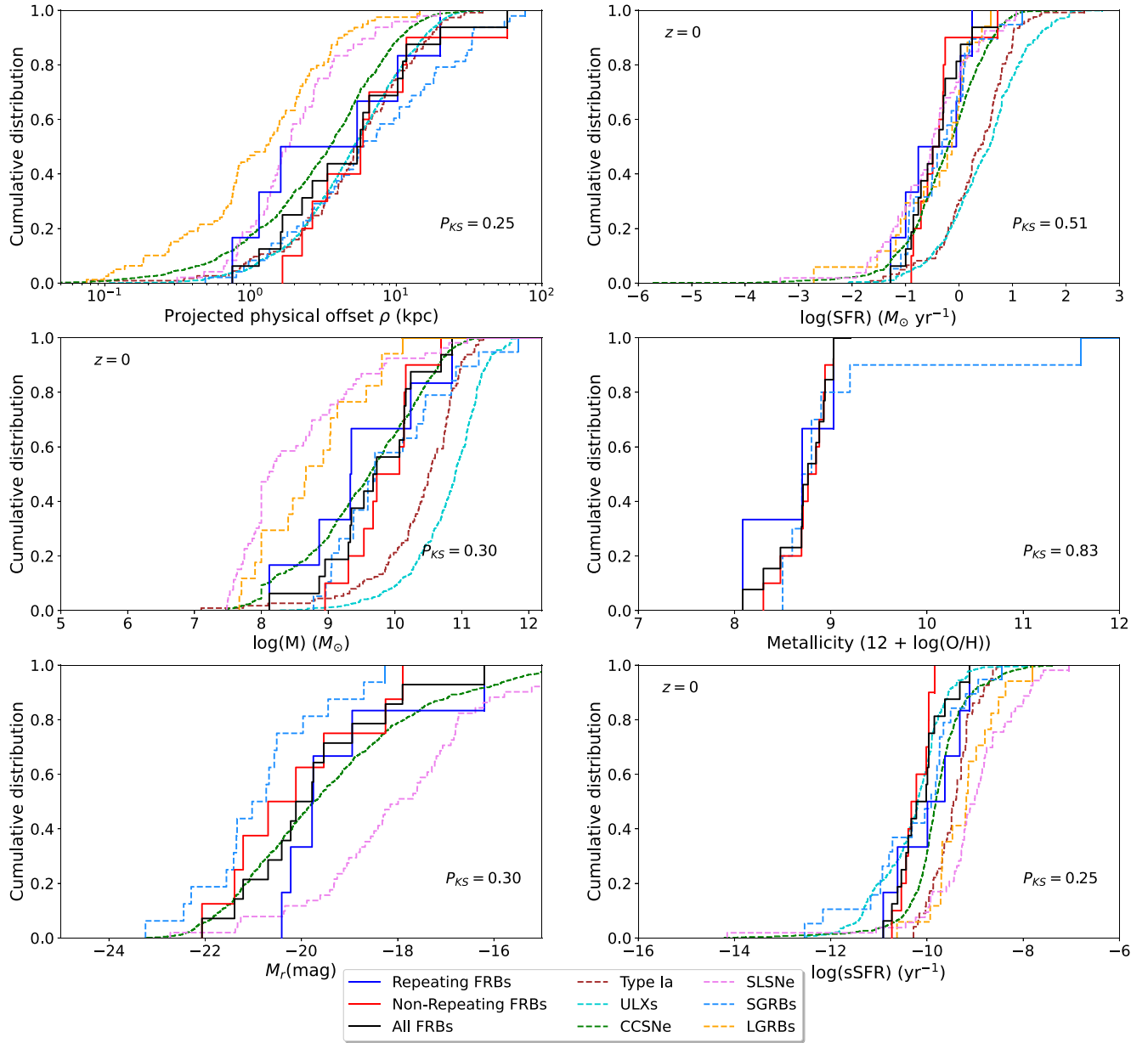


Figure 9. Cumulative distributions of the projected physical offsets, SFRs, stellar masses, metallicities, absolute r -band magnitudes and sSFRs for repeating (blue), nonrepeating (red), and combined (black) FRB host population compared with ultra-luminous X-ray (ULX) sources (cyan), short (light blue), and long (orange) gamma-ray bursts, and core-collapse (CC; green), superluminous (SL; magenta), and Type Ia (brown) supernovae (SNe). The data for these transients are taken from the literature listed in Table 3. The p -value for the KS test between the repeating and nonrepeating population is listed on the right side of each plot. We also summarize the p -values for KS tests between FRB populations and their respective transients in Table 4.

Table 3

Literature References of the Data Used for Various Transients in This Work

Transient Type	Literature References
ULXs ^a	Kovlakas et al. (2020)
SGRBs	Leibler & Berger (2010), Fong et al. (2010), Fong & Berger (2013), Berger (2014)
LGRBs	Blanchard et al. (2016), Taggart & Perley (2021)
CCSNe	Schulze et al. (2020)
SLSNe	Schulze et al. (2020), Taggart & Perley (2021)
Type Ia SNe	Lampeitl et al. (2010), Uddin et al. (2020)

Note.

^a Excluding unreliable data, nuclear sources, and sources with X-ray luminosities $< 10^{39}$ erg s⁻¹.

populations (repeating and nonrepeating) with the host galaxy properties of other transients (see Figure 9). We also included Type Ia supernovae—a proxy for the AIC of WD stars, which have been suggested as possible FRB progenitors (Margalit et al. 2019; Kirsten et al. 2021). Table 3 represents the data from the literature that has been used in this study for all these transients. We used the method described in Bochenek et al. (2020) to correct for redshift evolution by scaling the stellar masses and SFRs of host galaxies of FRBs and other transients to be statistically representative of $z = 0$ galaxies.

While the distribution of projected physical offsets for ULXs and Type Ia supernovae are statistically consistent with those of FRBs, their host galaxies are often more massive and star-forming, i.e., a mean of $\log(M_*) = 10.4 M_\odot$ and $10.8 M_\odot$, $\text{SFR} = 6.2 M_\odot \text{yr}^{-1}$ and $11.7 M_\odot \text{yr}^{-1}$ for the hosts of Type Ia

Table 4

P-values for Two-sample 1D KS After Comparing the Distributions of Various Properties (Column 1) of the Hosts of FRBs (All Together and Separated by Repeating and On–Off Host Population) with Those of Galaxies Hosting ULXs, SGRBs, LGRBs, SLSNe, CCSNe, and Type Ia SN

Property	FRB Type	Transients					
		ULXs	SGRBs	LGRBs	SLSNe	CCSNe	Type Ia
Offset	Rep.	0.28	0.44	0.18	0.37	0.82	0.28
	Nonrep.	0.97	0.57	0.00	0.02	0.25	0.99
	All	0.93	0.52	0.00	0.02	0.27	0.92
SFR	Rep.	0.01	0.93	0.96	0.86	0.65	0.03
	Nonrep.	0.00	0.26	0.07	0.18	0.04	0.00
	All	0.00	0.68	0.23	0.44	0.15	0.00
$\log(M)$	Rep.	0.00	0.36	0.29	0.06	0.73	0.02
	Nonrep.	0.00	0.64	0.00	0.00	0.33	0.00
	All	0.00	0.59	0.00	0.00	0.50	0.00
Z	Rep.	...	0.91
	Nonrep.	...	0.99
	All	...	0.84
M_r	Rep.	...	0.01	...	0.06	0.36	...
	Nonrep.	...	0.89	...	0.01	0.80	...
	All	...	0.06	...	0.00	0.73	...
sSFR	Rep.	0.32	0.75	0.25	0.05	0.70	0.34
	Nonrep.	0.46	0.08	0.00	0.00	0.00	0.00
	All	0.42	0.39	0.00	0.00	0.01	0.00

SN and ULXs, respectively. A possible caveat is that the ULX sample in the HECATE and the Chandra X-ray catalog is biased against low-mass galaxies due to various selection effects (Sridhar et al. 2021). However, we observe the sSFRs for ULX hosts to be similar to those of FRB hosts. Also, the majority of the properties of the hosts of SGRBs and CCSNe are very similar to FRB hosts, suggesting that the host population of FRB progenitors shares the same/similar characteristics to those of these transients. A KS test shows that the SFR distribution of LGRB hosts and SLSNe hosts are consistent with FRB hosts. However, we note that such events are common in dwarf galaxies with high sSFRs, as evident from the left-middle and right-bottom panels of Figure 9, which is not consistent with the overall FRB host population. Interestingly, while the results of our KS tests allow us to statistically rule out LGRB scenarios for all FRBs combined ($P_{\text{KS}} < 0.05$), we are unable to reject the hypothesis that the repeating FRB and LGRB hosts are drawn from the same continuous distribution. When comparing with SLSNe hosts, we found the physical offsets of the repeating FRBs ($P_{\text{KSR}} = 0.37$), stellar mass ($P_{\text{KSR}} = 0.06$), and r -band magnitude ($P_{\text{KSR}} = 0.06$) of their hosts to agree with that of SLSNe hosts. The p -values from our KS tests are presented in Table 4.

6.2. Comparison to the Galactic Source Population and Globular Clusters

The prevailing view currently associates FRBs with magnetars, whose extreme magnetic fields provide a reservoir of energy to produce FRBs (Metzger 2018; Lyutikov & Rafat 2019). With the detection of an FRB-like burst from SGR1935 + 2154, the association of some (low-luminosity) FRBs with magnetars has been observationally confirmed (Bochenek et al. 2020; CHIME/FRB Collaboration 2020). Following the analysis of Chrimes et al. (2021), we compared

the host-normalized offset distributions of low-mass X-ray binaries (LMXBs), high-mass X-ray binaries (HMXBs), pulsars and magnetars in the Milky Way with the updated FRB host sample—including all repeating and nonrepeating FRBs in the left panel of Figure 10. Based on our KS test, the offset distribution of only LMXBs in the Milky Way is consistent with that observed for FRBs in their host galaxies (95% confidence).

Recently, a repeating FRB20200120E originally associated with the galaxy M81 (Bhardwaj et al. 2021) has been precisely localized, by the EVN network, to a globular cluster (GC) system [PR95] 30244 in M81 (Kirsten et al. 2021). Motivated by this finding, we compared the host-normalized offset distributions of FRBs in our sample with globular clusters in late-type spirals and early-type elliptical galaxies in the right panel of Figure 10.

For the GCs in late-type galaxies, we used a sample of 340 high-quality GC candidates (of which 74 were confirmed using spectroscopy) associated with M81, identified in HST imaging (Nantais & Huchra 2010; Nantais et al. 2010). We note that the available data is dominated by a GC disk population with the majority of GCs within 10 kpc from the center of M81. We also used a sample of 390 GCs associated with the galaxy M31 (both disk and halo population) identified in images from the Wide Field Camera (WFCAM) on the United Kingdom Infrared Telescope and from the SDSS (Peacock et al. 2010). For early-type galaxies, we used the available GC data associated with an isolated elliptical galaxy NGC 821, extending up to 50 kpc from the center of the galaxy (Spitler et al. 2008). The sample consists of 306 GCs identified in the new imaging from the 3.5 m Wisconsin Indiana Yale NAO (WIYN) Mini-Mosaic imager, supplemented with the HST WFPC2 images. We also used a sample of 1828 GC candidates (of which 270 are confirmed using spectroscopy from Keck/DEIMOS) associated with the L_* elliptical galaxy NGC 4278,

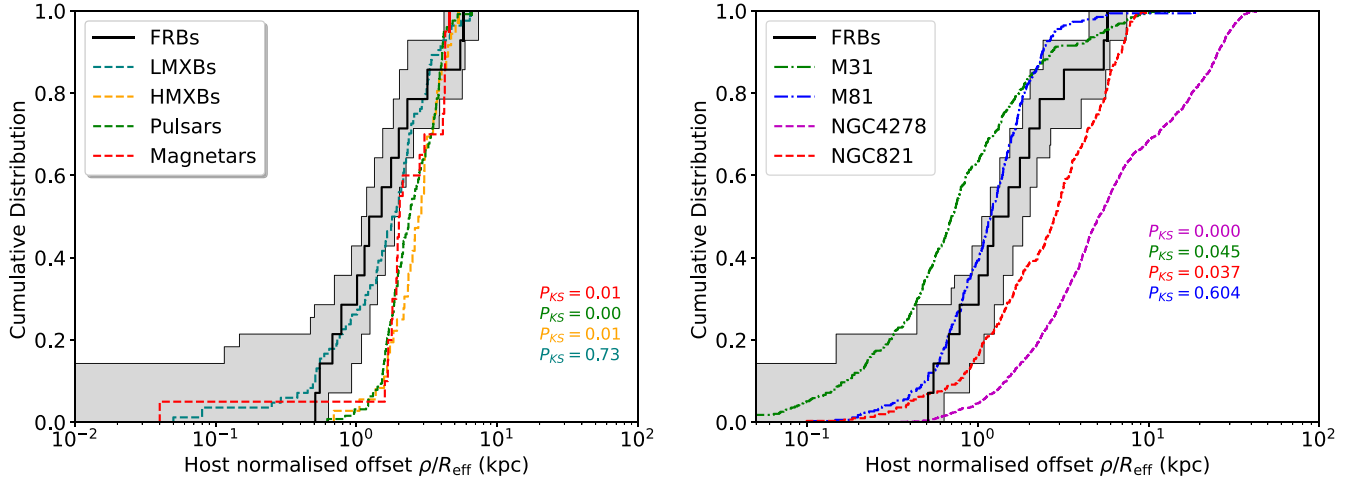


Figure 10. Left: cumulative distributions of the host-normalized offsets for FRBs compared with those of Galactic objects in the Milky Way galaxy. The data for various Galactic sources have been taken from Chimes et al. (2021). The gray-shaded region represents the 1σ uncertainty on the cumulative distribution function, accounting for uncertainties due to individual measurements and sample size. The p -values for KS test between Galactic sources and all FRBs are listed on the right side of the plot. Right: cumulative distributions of the host-normalized offsets for FRBs compared with offset distributions of globular clusters associated with M81, M31 (spiral late-type galaxies), NGC 821 (isolated elliptical galaxy), and NGC 4278 (L^* elliptical galaxy). The effective radii used for these galaxies are $R_{\text{eff}}(\text{M81}) = 3.5$ kpc (Bhardwaj et al. 2021), $R_{\text{eff}}(\text{M31}) = 7.2$ kpc (Savorgnan & Graham 2016), $R_{\text{eff}}(\text{NGC821}) = 5.1$ kpc (Pellegrini et al. 2007), and $R_{\text{eff}}(\text{NGC4278}) = 2.4$ kpc (Usher et al. 2013). The p -values for KS test between globular clusters and all FRBs are listed on the right side of the plot.

identified in HST/Advanced Camera for Surveys and wide-field Subaru/Suprime-Cam imaging (Usher et al. 2013). These selected galaxies have stellar masses and SFRs in the range $M_* = 10^{10.5} - 10^{11.5} M_\odot$ and $\text{SFR} = 0.01 - 1 M_\odot \text{ yr}^{-1}$, overlapping with the SFRs and high-mass end distribution of FRB host galaxies (Tamm et al. 2012; Forbes et al. 2016; Rahmani et al. 2016; Kokusho et al. 2017; Bhardwaj et al. 2021).

We compared the host-normalized offset distribution of FRBs in their hosts with that of globular clusters in selected galaxies and found that they are not consistent with being drawn from the same underlying distribution (95% confidence) except for M81 ($P_{\text{KS}} = 0.604$). This could be due to the fact that the M81 globular cluster data is incomplete and dominated by disk population.

A possible caveat in the above analysis is that the number of GCs scale with galaxy stellar mass, and our FRB host population spans four orders of magnitude in the stellar mass, i.e., $M_* = 10^8 - 10^{11} M_\odot$. We also repeated the KS test by selecting FRB hosts which had $M_* > 10^{10} M_\odot$ and found similar results, however with lower confidence of 80%. Furthermore, we note that our FRB host sample currently shows a deficiency of elliptical galaxies. A subset of FRBs in our sample were found to originate from or near the spiral arms of their hosts. Whether they are linked to the disk population of GCs is presently unknown and we are limited by the sensitivity of current telescopes. A much larger sample of precisely localized FRBs with high spatial observations of nearby hosts are needed to pursue this further.

7. Summary and Future Work

We have presented the localization of the sixth repeating FRB20180301A using the REALFAST system at the VLA and two apparently nonrepeating FRBs (FRB20191228A and FRB20200906A) discovered by ASKAP. With an updated sample of six repeating and 10 nonrepeating FRB host galaxies, we have conducted a differential analysis of global properties of the FRB host population. While the latest observations of FRBs from the CHIME/FRB project strongly

suggest that repeaters and single-burst sources arise from separate mechanisms and astrophysical sources (Pleunis et al. 2021), we did not find significant differences in their host populations. We observed FRB hosts to be moderately star-forming galaxies ($0.06 - 8 M_\odot \text{ yr}^{-1}$), with masses offset from the star-forming main sequence. The majority of FRB hosts lie in the star-forming and LINER region of the BPT diagram. As a low-metallicity dwarf galaxy, the host of FRB20121102A continues to be an outlier in the sample. Furthermore, we observe no persistent radio emission colocated with the bursts in our radio follow-up observations of FRBs 20180301A, 20191228A, and 20200906A. We note that the derived 3σ upper limits on the luminosity of these sources are lower than the luminosity of the FRB20121102A persistent source ($2.1 \times 10^{22} \text{ W Hz}^{-1}$ at 1.4 GHz; Ofek 2017), indicating that these bursts might originate from less extreme environments.

We find that THE FRBs in our sample do not track the stellar mass and in general are not hosted in old, red, and dead galaxies which have old stellar populations. The dearth of FRBs in the massive red galaxies suggest that FRBs are not solely produced in channels with a large average delay between star formation and the FRB source formation, such as magnetars formed via compact object-related systems, including NS mergers, or the AIC of a WD to a NS. Current data supports a mix of prompt (core-collapse SNe) and delayed channels for producing FRB progenitors, suggesting that they are drawn from the general stellar population rather than an exotic and rare subpopulation. Furthermore, FRB hosts do not follow the sSFRs of main-sequence star-forming galaxies, nor do they track the SFRs of field galaxies in the nearby universe.

When comparing the properties of FRB host galaxies with those of other transients, we find the host galaxies of ULXs and Type Ia supernovae to be more massive and star-forming than FRBs. The hosts of CCSNe and SGRBs are similar to FRB hosts in terms of their stellar masses, SFRs, projected physical offsets, absolute r -band magnitudes, and sSFRs. While from the host galaxy considerations, we could statistically rule out LGRBs and SLSNe as progenitor scenarios for all FRBs

combined, we found some similarities between the repeating FRB host population and hosts of LGRBs and SLSNe. These may be attributed to either the small sample size or the effect of the outlier FRB20121102A host galaxy on the overall repeating FRB host population. We also note that one is more likely to find an extreme value under the null hypothesis with more KS tests.

Driven by the studies and findings of Chrimes et al. (2021) and Kirsten et al. (2021), we compared the physical offsets of FRBs in their hosts with those of Galactic sources such as pulsars, magnetars, X-ray binaries in the Milky Way, and globular clusters in late- and early-type galaxies. According to our KS tests, the Galactic source offset distributions of the NS population and HMXBs are different, while LMXBs are indistinguishable from the observed FRB offset distribution (95% confidence). We also show that FRBs are positioned in their host galaxies in a way that is mostly not comparable to globular clusters found in late-type spiral and early-type elliptical galaxies.

Lastly, in the future, observations of a much larger sample of nearby FRB hosts will be ideal for progenitor model studies as these will allow the high-spatial-resolution analysis of FRB environments in their host galaxies.

All of the data and the majority of the software used for the host analysis are available at <https://github.com/FRBs/FRB>.

S.B. would like to thank Themiya Nanayakkara, Arash Bahramian, and Kristen Dage for useful discussions. R.M.S. acknowledges support from the Australian Research Council Future Fellowship FT190100155. K.E.H. acknowledges support by a Postdoctoral Fellowship Grant (217690–051) from The Icelandic Research Fund. K.A. acknowledges support from NSF grant No. AAG-1714897. L.M. acknowledges the receipt of an MQ-RES scholarship from Macquarie University. S.B.S. acknowledges support from NSF grant No. AAG-1714897. She is a CIFAR Azrieli Global Scholar in the Gravity and the Extreme Universe program, which helped support J.S. for this project. A.T.D. is the recipient of an Australian Research Council Future Fellowship (FT150100415). W.F. acknowledges support by the National Science Foundation under grant Nos. AST-1814782, AST-1909358, and CAREER grant No. AST-2047919. C.J.L. acknowledges support from the National Science Foundation under grant No. 2022546. N.T. acknowledges support by FONDECYT grant No. 11191217. K.J.L. is supported by CAS XDB23010200, Max-Planck Partner Group, National SKA program of China grant No. 2020SKA0120100, NSFC grant No. 11690024, CAS Cultivation Project for FAST Scientific. The NANOGrav project receives support from the National Science Foundation (NSF) Physics Frontiers Center, award number 1430284. Part of this research was carried out at the Jet Propulsion Laboratory, California Institute of Technology, under a contract with the National Aeronautics and Space Administration. Authors S.S., N.T., J.X.P., and K.G.L. as members of the Fast and Fortunate for FRB Follow-up team, acknowledge support from NSF grant Nos. AST-1911140 and AST-1910471. The Australian Square Kilometre Array Pathfinder and Australia Telescope Compact Array (ATCA) are part of the Australia Telescope National Facility, which is managed by CSIRO. Operation of ASKAP is funded by the Australian Government with support from the National

Collaborative Research Infrastructure Strategy. ASKAP uses the resources of the Pawsey Supercomputing Centre. Establishment of ASKAP, the Murchison Radio-astronomy Observatory and the Pawsey Supercomputing Centre are initiatives of the Australian Government, with support from the Government of Western Australia and the Science and Industry Endowment Fund. We acknowledge the Wajarri Yamatji as the traditional owners of the Murchison Radio-astronomy Observatory site. We acknowledge the Gomeroi people as the traditional owners of the Paul Wild (ATCA) Observatory site. The National Radio Astronomy Observatory is a facility of the National Science Foundation operated under cooperative agreement by Associated Universities, Inc. Spectra were obtained at the W. M. Keck Observatory, which is operated as a scientific partnership among Caltech, the University of California, and the National Aeronautics and Space Administration (NASA). W. M. Keck Observatory and MMT Observatory access was in part supported by Northwestern University and the Centre for Interdisciplinary Exploration and Research in Astrophysics (CIERA). The Keck Observatory was made possible by the generous financial support of the W. M. Keck Foundation. The authors recognize and acknowledge the very significant cultural role and reverence that the summit of Maunakea has always had within the indigenous Hawaiian community. We are most fortunate to have the opportunity to conduct observations from this mountain. Observations reported here were obtained at the MMT Observatory, a joint facility of the University of Arizona and the Smithsonian Institution. Based on observations collected at the European Southern Observatory under ESO program 0105.A-0687(A). Based on observations obtained at the international Gemini Observatory, a program of NSF's NOIRLab, which is managed by the Association of Universities for Research in Astronomy (AURA) under a cooperative agreement with the National Science Foundation on behalf of the Gemini Observatory partnership: the National Science Foundation (United States), National Research Council (Canada), Agencia Nacional de Investigación y Desarrollo (Chile), Ministerio de Ciencia, Tecnología e Innovación (Argentina), Ministério da Ciência, Tecnologia, Inovações e Comunicações (Brazil), and Korea Astronomy and Space Science Institute (Republic of Korea). The Gemini data were obtained from program GS-2020B-Q-138, and were processed using the Data Reduction for Astronomy from Gemini Observatory North and South (DRAGONS) package.

Software: PYSE (Spreeuw et al. 2018), ESOReflex (Freudling et al. 2013), Montage (Jacob et al. 2010), Source-Extractor (Bertin & Arnouts 1996), Astropy (Robitaille et al. 2013), Burstfit (Aggarwal et al. 2021a), Scipy (Jones et al. 2001), CASA (McMullin et al. 2007), CIGALE (Noll et al. 2009), pPXF (Cappellari 2017).

Appendix

The spectrum of the new FRB hosts in this paper and newly obtained data for FRB20200430A are shown in Figure A1. Table A1 lists the nebular line measurements of FRB hosts that are used in the BPT diagram. We have also updated the previously reported Pan-STARRS photometric measurements (PSFMag) for the hosts of FRB20190523A, FRB20190714A, and FRB20200430A to Kron Mag and redid the SED fitting in CIGALE using the method described in Heintz et al. (2020).

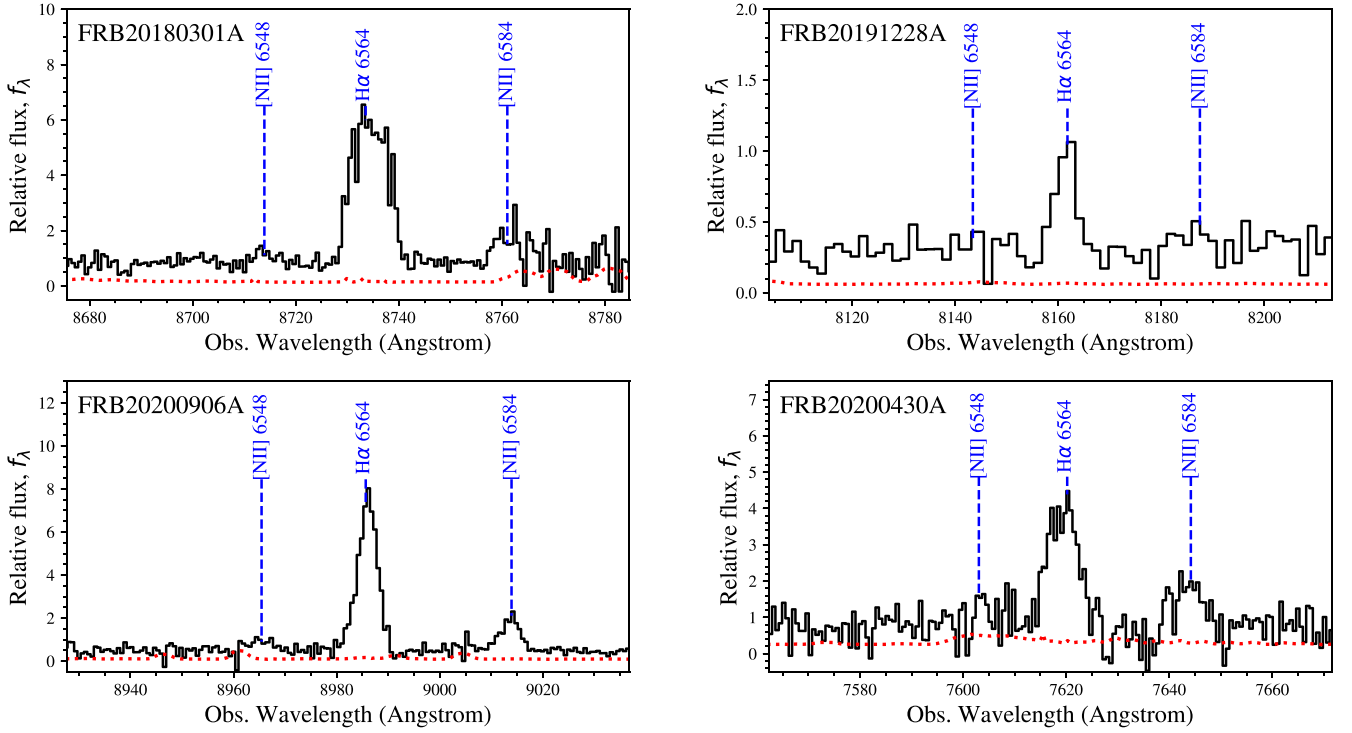


Figure A1. A zoomed in version of the optical spectrum of the host of FRB20180301A, FRB20191228A, FRB20200906A and FRB20200430A.

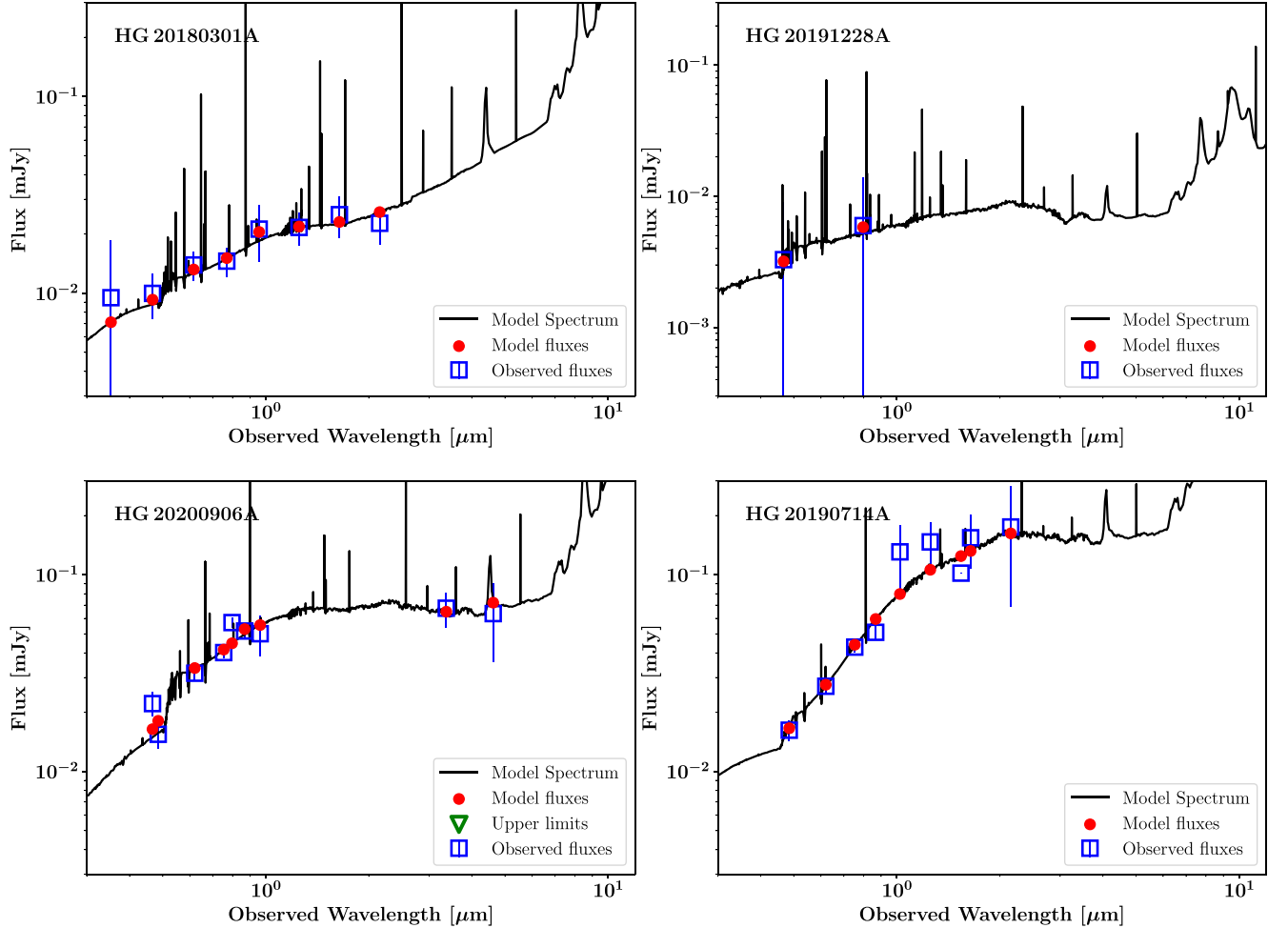


Figure A2. SED models for the host galaxies of FRB20180301A, FRB20191228A, FRB20200906A, FRB20190714A. The best-fit SED models from CIGALE are shown as solid black lines, the observed magnitudes (corrected for Galactic extinction and converted into fluxes) as blue squares, and the model fluxes as red dots. In all models, the redshift has been fixed to the redshift of respective host galaxies.

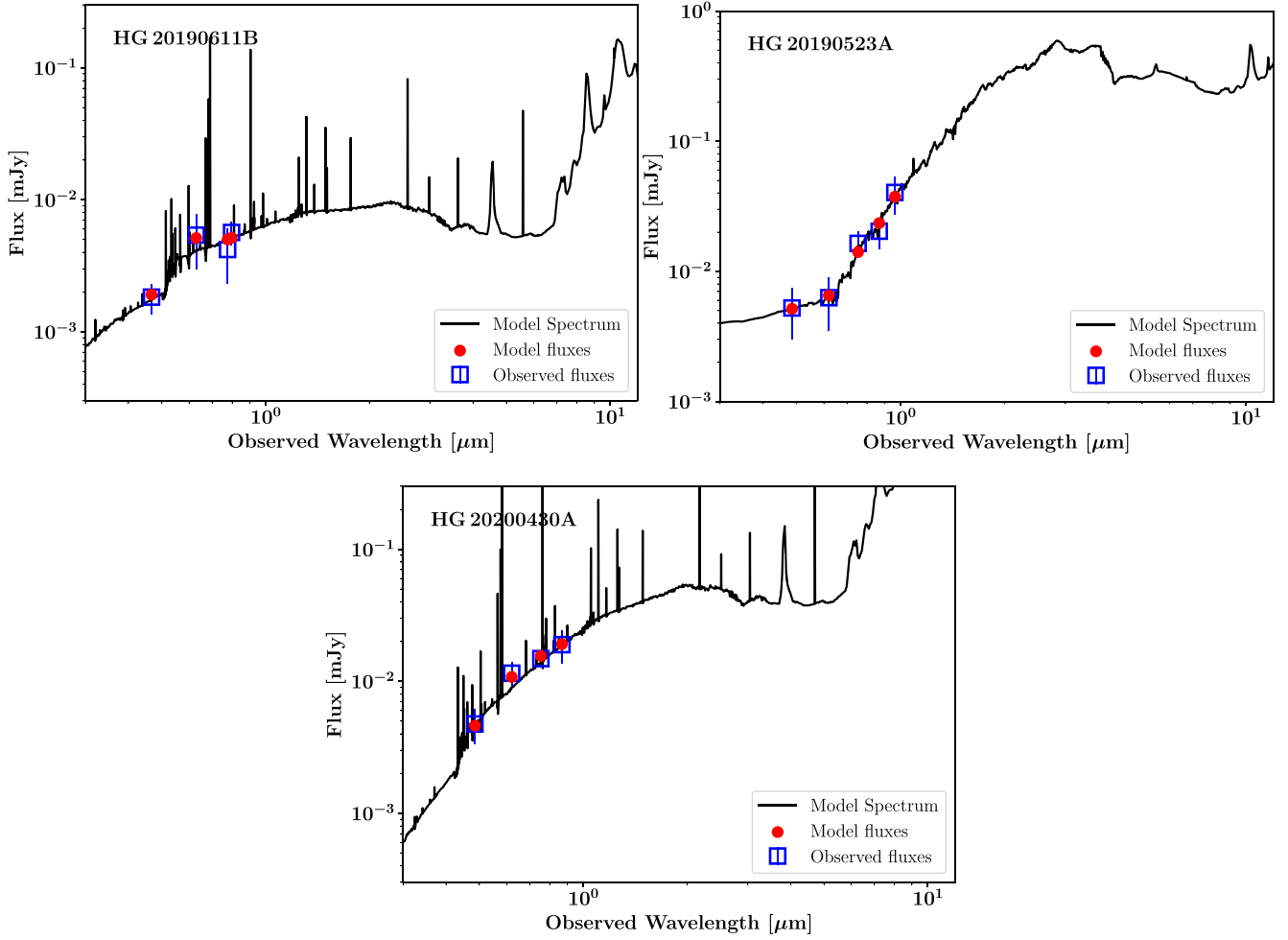


Figure A3. SED models for the host galaxies of FRB20190611B, FRB20190523A, and FRB20200430A.

Table A1
Nebular Line Emission Measurements in Units of $10^{-16} \text{ erg s}^{-1} \text{ cm}^{-2}$

FRB	H α	H β	[N II]	[O III]
FRB20121102A	2.61 ± 0.04	0.96 ± 0.09	<0.12	4.38 ± 0.08
FRB20180301A	16.97 ± 0.18	7.77 ± 0.61	4.32 ± 0.32	12.75 ± 0.65
FRB20180916B	40.27 ± 0.25	...	15.24 ± 0.24	71.62 ± 0.60
FRB20180924B	2.79 ± 0.03	0.72 ± 0.02	1.94 ± 0.03	0.79 ± 0.02
FRB20190102C	5.66 ± 0.17	1.90 ± 0.17	1.69 ± 0.19	3.80 ± 0.27
FRB20190608B	27.65 ± 0.41	8.37 ± 0.33	18.32 ± 0.38	14.95 ± 0.44
FRB20190611B	0.49 ± 0.05	0.12 ± 0.03	0.12 ± 0.04	0.18 ± 0.04
FRB20190711A	...	0.26 ± 0.05
FRB20190714A	3.89 ± 0.03	0.97 ± 0.03	1.70 ± 0.03	0.31 ± 0.03
FRB20191001A	27.38 ± 0.26	5.01 ± 0.30	13.91 ± 0.19	3.62 ± 0.35
FRB20191228A	0.30 ± 0.02	0.02 ± 0.02	0.08 ± 0.02	0.13 ± 0.03
FRB20200430A	4.27 ± 0.15	1.15 ± 0.21	2.02 ± 0.20	1.17 ± 0.25
FRB20200906A	6.49 ± 0.07	4.25 ± 0.14	1.80 ± 0.06	5.38 ± 0.17
FRB20201124A	$56.9^{+14.9}_{-9.9}$	$12.3^{+3.0}_{-2.3}$	$25.3^{+6.0}_{-4.7}$	$3.8^{+2.1}_{-1.1}$

Note. The data for FRB20171020A and FRB20201124A are taken from Mahony et al. (2018) and Fong et al. (2021), respectively.

Table A2
Results for FRB Associations

FRB	R.A. _{cand}	Decl. _{cand}	θ	ϕ	m	Filter	P^c	$P(O)$	$P(O x)$
FRB20121102A	82.9945	33.1479	0.2	0.28	23.52	GMOS_N_i	0.0039	0.0245	1.0000
FRB20180916A	29.5012	65.7148	7.7	3.03	16.16	GMOS_N_r	0.0005	0.8200	1.0000
FRB20180924B	326.1054	−40.9002	0.8	1.31	21.32	VLT_FORS2_g	0.0119	0.8723	0.9894
FRB20181112A	327.3486	−52.9709	0.4	0.67	21.49	VLT_FORS2_I	0.0622	0.0784	0.6678
FRB20190102C	322.4149	−79.4756	0.5	0.86	20.73	VLT_FORS2_I	0.0056	0.8425	1.0000
FRB20190523A	207.0642	72.4706	3.4	0.71	22.13	LRIS_R	0.1158	0.1974	0.8154
FRB20190608B	334.0203	−7.8988	2.5	1.66	17.60	VLT_FORS2_I	0.0005	0.9930	1.0000
FRB20190611B	320.7429	−79.3973	2.0	0.50	22.35	GMOS_S_i	0.0407	0.3322	0.9741
FRB20190614D	65.0743	73.7068	1.3	0.41	24.01	LRIS_I	0.0552	0.1944	0.5825
FRB20190711A	329.4194	−80.3581	0.5	0.46	22.93	GMOS_S_i	0.0172	0.4782	0.9937
FRB20190714A	183.9795	−13.0212	1.2	0.95	19.48	VLT_FORS2_I	0.0014	0.7993	1.0000
FRB20191001A	323.3525	−54.7487	4.2	1.36	17.82	VLT_FORS2_I	0.0010	0.5075	0.5980
FRB20200430A	229.7064	12.3766	0.4	0.72	21.18	LRIS_I	0.0047	0.9379	1.0000
FRB20191228A	344.4307	−29.5940	2.1	0.49	21.92	VLT_FORS2_I	0.0251	0.5596	1.0000
FRB20200906A	53.4958	−14.0833	1.6	1.51	20.70	VLT_FORS2_g	0.0106	0.8997	1.0000
FRB20180301A	93.2269	4.6704	2.3	0.92	22.07	GMOS_S_r	0.0387	0.7154	0.9993

Furthermore, we obtained new VLT/FORS2 measurements for the host of FRB20190611B. The best-fitting models for these hosts and new FRBs introduced in this work are presented in

Figures A2 and A3, and the updated derived measurements are shown in Table A3. The new and updated photometry is presented in Table A4.

Table A3
Host Galaxies of Six Repeating and Ten Nonrepeating FRBs Used in This Work, for which PATH Posterior Probability is >90%

S.No	FRB	z	Rep	Offset (kpc)	$R_{\text{eff}}^{\text{a}}$ (kpc)	Mass ($10^{10} M_{\odot}$)	SFR ($M_{\odot} \text{ yr}^{-1}$)	$\log(\text{sSFR})$ (yr^{-1})	M_r	$u - r$	Z
1	FRB20121102A	0.1927	y	0.8 ± 0.1	0.66 ± 0.03	0.01 ± 0.01	0.15 ± 0.04	-8.99	-16.20 ± 0.08	1.49 ± 0.18	8.08
2	FRB20180301A	0.3304	y	10.2 ± 3.0	5.80 ± 0.20	0.23 ± 0.06	1.93 ± 0.58	-9.08	-20.18 ± 0.07	0.90 ± 0.11	8.70
3	FRB20180916B	0.0337	y	5.4 ± 0.0	3.57 ± 0.36	0.22 ± 0.03	0.06 ± 0.02	-10.58	-19.46 ± 0.05	1.53 ± 0.06	...
4	FRB20180924B	0.3212	n	3.4 ± 0.8	2.75 ± 0.10	1.32 ± 0.51	0.88 ± 0.26	-10.18	-20.81 ± 0.05	1.78 ± 0.15	8.93
5	FRB20190102C	0.2912	n	2.3 ± 4.2	4.43 ± 0.51	0.47 ± 0.54	0.86 ± 0.26	-9.74	-19.87 ± 0.06	1.44 ± 0.15	8.70
6	FRB20190608B	0.1178	n	6.5 ± 0.8	2.84 ± 0.23	1.16 ± 0.28	0.69 ± 0.21	-10.22	-21.22 ± 0.05	1.40 ± 0.09	8.85
7	FRB20190611B	0.3778	n	11.7 ± 5.8	2.15 ± 0.11	0.35 ± 0.70	0.27 ± 0.08	-10.11	-19.29 ± 0.10	1.29 ± 0.18	8.71
8	FRB20190711A	0.5220	y	1.6 ± 4.5	2.94 ± 0.17	0.08 ± 0.03	0.42 ± 0.12	-9.29	-19.01 ± 0.08	0.95 ± 0.16	...
9	FRB20190714A	0.2365	n	2.7 ± 1.8	3.94 ± 0.05	1.42 ± 0.55	0.65 ± 0.20	-10.34	-20.37 ± 0.05	1.51 ± 0.28	9.03
10	FRB20191001A	0.2340	n	11.1 ± 0.8	5.55 ± 0.03	4.64 ± 1.88	8.06 ± 2.42	-9.76	-22.13 ± 0.05	1.67 ± 0.19	8.94
11	FRB20191228A	0.2432	n	5.7 ± 3.3	1.78 ± 0.06	0.54 ± 0.60	0.50 ± 0.15	-10.03	-18.26 ± 0.05	2.13 ± 0.74	8.48
12	FRB20200430A	0.1608	n	1.7 ± 2.2	1.64 ± 0.53	0.21 ± 0.11	0.26 ± 0.08	-9.89	-18.25 ± 0.05	2.08 ± 0.30	8.88
13	FRB20200906A	0.3688	n	5.9 ± 2.0	7.58 ± 0.06	1.33 ± 0.37	0.48 ± 0.14	-10.44	-21.49 ± 0.05	1.22 ± 0.11	8.76
14	FRB20171020A ^b	0.0087	n	0.09	0.13	-9.84	-17.9	...	8.30
15	FRB20200120E ^b	0.0008	y	20.1 ± 3.0	3.5	7.20 ± 1.70	0.89 ± 0.27	-10.91	-19.78	2.77 ± 0.00	...
16	FRB20201124A ^b	0.0980	y	1.3 ± 0.1	...	$1.70^{+0.08}_{-0.11}$	$2.12^{+0.69}_{-0.28}$	-9.90	-20.41 ± 0.03	2.06 ± 0.55	9.03
...	FRB20190523A	0.6600	n	27.2 ± 22.6	3.28 ± 0.18	46.49 ± 35.51	0.09 ± 0.03	-12.74	-22.69 ± 0.14	2.20 ± 0.22	...

Notes. We have also added the most probable host of FRB20171020A (Mahony et al. 2018) in our sample including the published host of repeating FRB20200120E (Bhardwaj et al. 2021) and FRB20201124A (Fong et al. 2021).

^a Isophotal effective half-light radii are used for a sample of FRB hosts published in Mannings et al. (2020). For remaining hosts, effective radii derived from GALFIT are used.

^b Host properties are taken from Mahony et al. (2018), Bhardwaj et al. (2021), and Fong et al. (2021). The observed magnitudes for FRB20171020A, FRB20200120E, and FRB20201124A are approximated as rest-frame magnitudes because of their low redshifts.








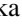






Table A4

Photometric Measurements for a Sample of New FRBs in This Work and Updated Pan-STARRS Measurements for Old FRBs Published in Heintz et al. (2020)

Filter	FRB20180301A	FRB20191228A	FRB20200906A	FRB20190523A	FRB20190611B	FRB20190714A	FRB20200430A
NOT _u	21.46 ± 0.30
NOT _g	21.40 ± 0.09
NOT _r	21.04 ± 0.06
NOT _i	20.99 ± 0.06
NOT _z	20.59 ± 0.11
Pan-STARRS _g	20.93 ± 0.05	22.10 ± 0.14	...	20.88 ± 0.04	22.21 ± 0.10
Pan-STARRS _r	20.15 ± 0.03	21.91 ± 0.15	...	20.32 ± 0.03	21.25 ± 0.07
Pan-STARRS _i	19.89 ± 0.02	20.86 ± 0.08	...	19.82 ± 0.02	20.97 ± 0.05
Pan-STARRS _z	19.62 ± 0.03	20.63 ± 0.09	...	19.63 ± 0.03	20.71 ± 0.10
Pan-STARRS _y	19.65 ± 0.08	19.88 ± 0.11	...	19.43 ± 0.06	...
VLT/FORS2 _g	...	22.61 ± 0.50	20.54 ± 0.05	...	23.24 ± 0.09	Heintz et al. (2020)	...
VLT/FORS2 _i	...	21.96 ± 0.40	19.51 ± 0.02	...	22.02 ± 0.07	Heintz et al. (2020)	...
MMT/MMRS _J	20.56 ± 0.07
MMT/MMRS _H	20.40 ± 0.08
MMT/MMRS _K	20.51 ± 0.08
WISE _{W1}	16.65 ± 0.07
WISE _{W2}	16.08 ± 0.14
WISE _{W3}	12.42 ± 0.49
WISE _{W4}	9.01

Note. All photometry have been corrected for Galactic extinction.

ORCID iDs

Shivani Bhandari  <https://orcid.org/0000-0003-3460-506X>
Kasper E. Heintz  <https://orcid.org/0000-0002-9389-7413>
Kshitij Aggarwal  <https://orcid.org/0000-0002-2059-0525>
Lachlan Marnoch  <https://orcid.org/0000-0003-1483-0147>
Cherie K. Day  <https://orcid.org/0000-0002-8101-3027>
Jessica Sydnor  <https://orcid.org/0000-0002-3360-9299>
Sarah Burke-Spolaor  <https://orcid.org/0000-0003-4052-7838>
Casey J. Law  <https://orcid.org/0000-0002-4119-9963>
J. Xavier Prochaska  <https://orcid.org/0000-0002-7738-6875>
Nicolas Tejos  <https://orcid.org/0000-0002-1883-4252>
Keith W. Bannister  <https://orcid.org/0000-0003-2149-0363>
Bryan J. Butler  <https://orcid.org/0000-0002-5344-820X>
R. D. Ekers  <https://orcid.org/0000-0002-3532-9928>
Chris Flynn  <https://orcid.org/0000-0002-4796-745X>
Wen-fai Fong  <https://orcid.org/0000-0002-7374-935X>
Clancy W. James  <https://orcid.org/0000-0002-6437-6176>
Elizabeth K. Mahony  <https://orcid.org/0000-0002-5053-2828>
Stuart D. Ryder  <https://orcid.org/0000-0003-4501-8100>
Elaine M. Sadler  <https://orcid.org/0000-0002-1136-2555>
Ryan M. Shannon  <https://orcid.org/0000-0002-7285-6348>
JinLin Han  <https://orcid.org/0000-0002-9274-3092>
Bing Zhang  <https://orcid.org/0000-0002-9725-2524>

References

- Agarwal, D., Aggarwal, K., Burke-Spolaor, S., Lorimer, D. R., & Garver-Daniels, N. 2020, *MNRAS*, **497**, 1661
Aggarwal, K., Agarwal, D., Lewis, E. F., et al. 2021a, *ApJ*, **922**, 115
Aggarwal, K., Budavári, T., Deller, A. T., et al. 2021b, *ApJ*, **911**, 95
Amiri, M., Andersen, B. C., Bandura, K., et al. 2021, *ApJS*, **257**, 59
Ai, S., Gao, H., & Zhang, B. 2021, *ApJL*, **906**, L5
Baldwin, J. A., Phillips, M. M., & Terlevich, R. 1981, *PASP*, **93**, 5
Bannister, K., Zackay, B., Qiu, H., James, C., & Shannon, R. 2019a, *FREDDA: A Fast, Real-time Engine for De-dispersing Amplitudes*, Astrophysics Source Code Library, ascl:1906.003
Bannister, K. W., Deller, A. T., Phillips, C., et al. 2019b, *Sci*, **365**, 565
Berger, E. 2014, *ARA&A*, **52**, 43
Berriman, G. B., & Good, J. C. 2017, *PASP*, **129**, 058006
Bertin, E., & Arnouts, S. 1996, *A&AS*, **117**, 393
Bhandari, S., Bannister, K. W., Lenc, E., et al. 2020, *ApJL*, **901**, L20
Bhandari, S., & Flynn, C. 2021, *Univ*, **7**, 85
Bhandari, S., Sadler, E. M., Prochaska, J. X., et al. 2020, *ApJL*, **895**, L37
Bhardwaj, M., Gaensler, B. M., Kaspi, V. M., et al. 2021, *ApJL*, **910**, L18
Blanchard, P. K., Berger, E., & Fong, W.-F. 2016, *ApJ*, **817**, 144
Bochenek, C. D., Ravi, V., Belov, K. V., et al. 2020, *Natur*, **587**, 59
Bochenek, C. D., Ravi, V., & Dong, D. 2021, *ApJL*, **907**, L31
Bothwell, M. S., Kennicutt, R. C., Johnson, B. D., et al. 2011, *MNRAS*, **415**, 1815
Caleb, M., Stappers, B. W., Rajwade, K., & Flynn, C. 2019, *MNRAS*, **484**, 5500
Cappellari, M. 2017, *MNRAS*, **466**, 798
Chabrier, G. 2003, *PASP*, **115**, 763
Chatterjee, S., Law, C. J., Wharton, R. S., et al. 2017, *Natur*, **541**, 58
CHIME/FRB Collaboration, Andersen, B. C., Bandura, K. M., et al. 2020, *Natur*, **587**, 54
Chittidi, J. S., Simha, S., Mannings, A., et al. 2021, *ApJ*, **922**, 173
Chrimes, A. A., Levan, A. J., Groot, P. J., Lyman, J. D., & Nelemans, G. 2021, *MNRAS*, **508**, 1929
Cid Fernandes, R., Stasińska, G., Schlickmann, M. S., et al. 2010, *MNRAS*, **403**, 1036
Condon, J. J., Cotton, W. D., Greisen, E. W., et al. 1998, *AJ*, **115**, 1693
Davidzon, I., Ilbert, O., Laigle, C., et al. 2017, *A&A*, **605**, A70
Day, C. K., Deller, A. T., James, C. W., et al. 2021, *PASA*, **38**, e050
Day, C. K., Deller, A. T., Shannon, R. M., et al. 2020, *MNRAS*, **497**, 3335
Fong, W., & Berger, E. 2013, *ApJ*, **776**, 18
Fong, W., Berger, E., & Fox, D. B. 2010, *ApJ*, **708**, 9
Fong, W.-f., Dong, Y., Leja, J., et al. 2021, *ApJL*, **919**, L23
Fonseca, E., Andersen, B. C., Bhardwaj, M., et al. 2020, *ApJL*, **891**, L6
Forbes, D. A., Sinpetru, L., Savorgnan, G., et al. 2016, *MNRAS*, **464**, 4611
Freudling, W., Romaniello, M., Bramich, D. M., et al. 2013, *A&A*, **559**, 96
Gaia Collaboration, Brown, A. G. A., Vallenari, A., et al. 2018, *A&A*, **616**, A1
Gordon, D. 2018, AGU, **2018**, G42A-01
Gordon, Y. A., Boyce, M. M., O'Dea, C. P., et al. 2020, *RNAAS*, **4**, 175
Heintz, K. E., Prochaska, J. X., Simha, S., et al. 2020, *ApJ*, **903**, 152
Ilbert, O., Arnouts, S., Le Floc'h, E., et al. 2015, *A&A*, **579**, A2

- Jacob, J. C., Katz, D. S., Berriman, G. B., et al. 2010, Montage: An Astronomical Image Mosaicking Toolkit, *Astrophysics Source Code Library*, ascl:1010.036
- James, C. W. 2019, *MNRAS*, **486**, 5934
- Jones, E., Oliphant, T., & Peterson, P. 2001, SciPy: Open Source Scientific Tools for Python
- Kauffmann, G., Heckman, T. M., Tremonti, C., et al. 2003, *MNRAS*, **346**, 1055
- Kennicutt, R. C. J. 1998, *ARA&A*, **36**, 189
- Kewley, L. J., Dopita, M. A., Sutherland, R. S., Heisler, C. A., & Trevena, J. 2001, *ApJ*, **556**, 121
- Kirsten, F., Marcote, B., Nimmo, K., et al. 2021, arXiv:2105.11445
- Kokusho, T., Kaneda, H., Bureau, M., et al. 2017, *A&A*, **605**, A74
- Kovlakas, K., Zezas, A., Andrews, J. J., et al. 2020, *MNRAS*, **498**, 4790
- Lacy, M., Baum, S. A., Chandler, C. J., et al. 2020, *PASP*, **132**, 035001
- Lampeitl, H., Smith, M., Nichol, R. C., et al. 2010, *ApJ*, **722**, 566
- Law, C. J., Bower, G. C., Burke-Spolaor, S., et al. 2018, *ApJS*, **236**, 8
- Law, C. J., Butler, B. J., Prochaska, J. X., et al. 2020, *ApJ*, **899**, 161
- Lee, J. C., Gil de Paz, A., Tremonti, C., et al. 2009, *ApJ*, **706**, 599
- Leibler, C. N., & Berger, E. 2010, *ApJ*, **725**, 1202
- Li, Y., & Zhang, B. 2020, *ApJL*, **899**, L6
- Li, Y., Zhang, B., Nagamine, K., & Shi, J. 2019, *ApJL*, **884**, L26
- Lindgren, L., Hernández, J., Bombrun, A., et al. 2018, *A&A*, **616**, A2
- Luo, R., Wang, B. J., Men, Y. P., et al. 2020, *Natur*, **586**, 693
- Lyutikov, M., & Rafat, M. 2019, arXiv:1901.03260
- Macquart, J.-P., Bailes, M., Bhat, N. D. R., et al. 2010, *PASA*, **27**, 272
- Macquart, J. P., Prochaska, J. X., McQuinn, M., et al. 2020, *Natur*, **581**, 391
- Mahony, E. K., Ekers, R. D., Macquart, J.-P., et al. 2018, *ApJL*, **867**, L10
- Mannings, A. G., Fong, W.-f., Simha, S., et al. 2020, *ApJ*, **917**, 75
- Marcote, B., Nimmo, K., Hessels, J. W. T., et al. 2020, *Natur*, **577**, 190
- Margalit, B., Berger, E., & Metzger, B. D. 2019, *ApJ*, **886**, 110
- Margalit, B., & Metzger, B. D. 2018, *ApJL*, **868**, L4
- Martin, D. C., Wyder, T. K., Schiminovich, D., et al. 2007, *ApJS*, **173**, 342
- McMullin, J. P., Waters, B., Schiebel, D., Young, W., & Golap, K. 2007, in ASP Conf. Ser. 376, *Astronomical Data Analysis Software and Systems XVI*, ed. R. A. Shaw, F. Hill, & D. J. Bell (San Francisco, CA: ASP), 127
- Metzger, B. D. 2018, *NatAs*, **2**, 192
- Michilli, D., Seymour, A., Hessels, J. W. T., et al. 2018, *Natur*, **553**, 182
- Moustakas, J., Coil, A. L., Aird, J., et al. 2013, *ApJ*, **767**, 50
- Nantais, J. B., & Huchra, J. P. 2010, *AJ*, **139**, 2620
- Nantais, J. B., Huchra, J. P., McLeod, B., Strader, J., & Brodie, J. P. 2010, *AJ*, **139**, 1413
- Noll, S., Burgarella, D., Giovannoli, E., et al. 2009, *A&A*, **507**, 1793
- Ofek, E. O. 2017, *ApJ*, **846**, 44
- Palaniswamy, D., Li, Y., & Zhang, B. 2018, *ApJL*, **854**, L12
- Peacock, M. B., Maccarone, T. J., Knigge, C., et al. 2010, *MNRAS*, **402**, 803
- Pellegrini, S., Siemiginowska, A., Fabbiano, G., et al. 2007, *ApJ*, **667**, 749
- Pleunis, Z., Good, D. C., Kaspi, V. M., et al. 2021, *ApJ*, **923**, 1
- Price, D. C., Foster, G., Geyer, M., et al. 2019, *MNRAS*, **486**, 3636
- Prochaska, J. X., Macquart, J.-P., McQuinn, M., et al. 2019, *Sci*, **366**, 231
- Rahmani, S., Lianou, S., & Bamby, P. 2016, *MNRAS*, **456**, 4128
- Ravi, V. 2019, *NatAs*, **3**, 928
- Ravi, V., Catha, M., D’Addario, L., et al. 2019, *Natur*, **572**, 352
- Ravi, V., Law, C. J., Li, D., et al. 2021, arXiv:2106.09710
- Robitaille, T. P., Tollerud, E. J., Greenfield, P., et al. 2013, *A&A*, **558**, 9
- Safarzadeh, M., Prochaska, J. X., Heintz, K. E., & Fong, W.-F. 2020, *ApJL*, **905**, L30
- Savorgnan, G. A. D., & Graham, A. W. 2016, *ApJS*, **222**, 10
- Schulze, S., Yaron, O., Sollerman, J., et al. 2020, *ApJS*, **255**, 29
- Spitler, L. R., Forbes, D. A., Strader, J., Brodie, J. P., & Gallagher, J. S. I. 2008, *MNRAS*, **385**, 361
- Spreeuw, H., Swinbank, J., Molenaar, G., et al. 2018, PySE: Python Source Extractor for Radio Astronomical Images, *Astrophysics Source Code Library*, ascl:1805.026
- Sridhar, N., Metzger, B. D., Beniamini, P., et al. 2021, *ApJ*, **917**, 13
- Strateva, I., Ivezić, Ž., Knapp, G. R., et al. 2001, *ApJ*, **122**, 1861
- Taggart, K., & Perley, D. A. 2021, *MNRAS*, **503**, 3931
- Tamm, A., Tempel, E., Tenjes, P., Tihhonova, O., & Tuvikene, T. 2012, *A&A*, **546**, A4
- Tendulkar, S. P., Gil de Paz, A., Kirichenko, A. Y., et al. 2021, *ApJL*, **908**, L12
- Tendulkar, S. P., Kaspi, V. M., & Patel, C. 2016, *ApJ*, **827**, 59
- Uddin, S. A., Burns, C. R., Phillips, M. M., et al. 2020, *ApJ*, **901**, 143
- Usher, C., Forbes, D. A., Spitler, L. R., et al. 2013, *MNRAS*, **436**, 1172